Received: 18 April 2025 | Revised: 20 July 2025 | Accepted: 29 July 2025

DOI: 10.1111/jace.70168

Journal of the American Ceramic Society

RESEARCH ARTICLE

Understanding of alkali–silica reaction in lime-pozzolana mortar incorporating pumice and borosilicate

Adhora Tahsin[1] | **Ishrat Baki Borno**[1] | **Taehwan Kim**[2] | **Warda Ashraf**[1]

[1]Department of Civil Engineering, The University of Texas at Arlington, Arlington, Texas, USA

[2]Centre for Infrastructure Engineering and Safety, School of Civil and Environmental Engineering, University of New South Wales (UNSW), Sydney, NSW, Australia

Correspondence
Warda Ashraf, Department of Civil Engineering, The University of Texas at Arlington, Nedderman Hall, 416 Yates St., Arlington, TX 76019, USA.
Email: warda.ashraf@uta.edu

Funding information
Defense Advanced Research Projects Agency, Grant/Award Number: W911NF2010308

Abstract

To assess the efficacy of lime-calcined clay binder in mitigating alkali–silica reaction (ASR) deterioration, this study identifies potential reaction product formation mechanisms in 2-year-old alkaline solution-exposed mortar bars using X-ray diffraction, micro-computed tomography, scanning electron microscopy, and evaluates their influence on mortar performance. The bar samples exhibit only 0.02% ASR-induced expansion, ascribed to the high alumina incorporation from the binder matrix into the initially formed sodium silicate hydrate (N-S-H) gel, enhancing silica polymerization and eventually forming zeolites such as phillipsite and chabazite. These zeolites, with a (Na+K)/Si ratio of 0.2–0.5, can uptake alkali, thus reducing their availability for further reactions. The crystalline ASR product Na-shlykovite is also observed, coexisting with the zeolites and forming at their core. Additionally, pumice inclusion in the binder enhances its ASR mitigation capability by supplying additional alumina and accommodating reaction products within its internal voids, thereby preventing the propagation of shrinkage cracks into the binder matrix. Consequently, including pumice with borosilicate in lime-calcined clay mortar increased its compressive strength by 52% compared with using only borosilicate under prolonged alkaline conditions.

KEYWORDS

alkali–silica reaction, lime-calcined clay, Na-shlykovite, pumice, zeolite

1 | INTRODUCTION

With the increased stress on freshwater availability and consumption, cementitious composites prepared with seawater are gaining popularity. One concern regarding the use of seawater as mixing water is that the sodium (Na^+) and potassium (K^+) ions it contains can react with reactive aggregate, potentially making the resulting cementitious composites susceptible to alkali–silica reaction (ASR).[1–3] While ordinary Portland cement (OPC) mortars show vulnerability to ASR when mixed with seawater,[4] ancient Roman concrete, which also used seawater for mixing, shows extremely high resistance to ASR.[5] Ancient Roman marine concrete structures, made from volcanic ash and hydrated lime binding tuff or carbonate rock aggregates, have lasted over 2000 years, withstanding full immersion

in seawater or shoreline exposure.[6] The pozzolanic reaction between volcanic ash and hydrated lime is the prime contributor to the durability of this concrete.[5] Additionally, including pumice—a glassy, porous volcanic mineral[7,8]—helped prevent expansive ASR gel formation, which typically causes cracking and deformation in concrete.[9] The ASR prevention mechanism in Roman concrete includes alkaline fluids reacting in piers and breakwaters to precipitate phillipsite and Al-tobermorite minerals.[5] These minerals refine pore spaces, strengthen pumice bonds, and sequester alkali cations (Na^+ and K^+).[5] Inspired by Roman concrete, previous studies developed a similar binder using calcined clay, hydrated lime [$Ca(OH)_2$], and seawater.[10,11] In this system, lime serves as a binder material rather than a hydration product.[10,11] Calcining clay minerals like kaolinite and montmorillonite converts them into reactive aluminosilicates.[12] Through pozzolanic reactions with lime, the main hydration products formed include calcium alumina silicate hydrate (C-A-S-H) gel, geopolymer gel, and crystalline phases like ettringite and hydrocalumite.[10] Given this binder's similarity to Roman concrete,[13] further investigation is needed into this binder's durability under high-alkaline conditions and ASR mechanisms, using pumice as a reactive aggregate for comparison with the ancient material's durability.

Additionally, while extensive research has examined the ASR mechanism in various binders, including OPC, OPC with supplementary cementitious material (SCM) substitutions, and alkali activaated material (AAM), the understanding of such mechanisms in lime-pozzolana binders is yet to be explored. Therefore, this study examines the long-term mechanisms in forming and propagating ASR products within lime-calcined clay-based mortar containing pumice as fine aggregates. To evaluate the effectiveness of alumina (Al) availability and the internal porosity of volcanic pumice [14] in reducing ASR deterioration, borosilicate—a nonporous, silica-rich material—was used as a pumice substitute at 50% and 100%.[15] The accelerated mortar bar test was conducted per ASTM C1260, a widely accepted potential ASR detection method, within 16 days.[2,16,17] Progressive microstructural changes were also monitored over time, by storing the mortar bars for up to 2 years, with periodic evaluations performed at 7 days, 14 days, 6 months, and 2 years.

2 | BRIEF REVIEW ON ASR MECHANISM, CRACK DEVELOPMENT, AND MITIGATION BY AL INCORPORATION

Alkali–silica reaction (ASR) in concrete occurs as hydroxide ions (OH^-) from the alkaline pore solution instigate the metastable silica network dissolution in reactive aggregates, converting the siloxane group (≡Si–O–Si≡) into the silanol group (≡Si–OH).[18–21] This process eventually generates highly soluble silica (Si) species like $H_3SiO_4^-$ and $H_2SiO_4^{2-}$, which undergo an ion exchange process with available K^+ or Na^+ ions to form alkali silicates.[18,22] Subsequently, the available calcium (Ca^{2+}) ions in pore solution substitute for some of these alkalis, forming alkali–calcium–silicate hydrates.[21,23,24] As per Hou et al.[21] and Kim et al.,[22] higher Ca^{2+} availability influences the dissolved silica to initially form C-S-H; as $Ca(OH)_2$ is depleted, C-S-H shifts to C-(Na/K)-S-H and eventually forms alkali silicate hydrate (A–S–H).

The primary approaches for the expansion pressure by ASR gel resulting in concrete degradation involve crystallization pressure, osmosis, swelling pressure, or the electrical double layer.[25–27] Portlandite [$Ca(OH)_2$)] or Ca^{2+} ion presence in the pore solution plays an important role in imparting ASR expansion in the OPC matrix,[28] though their role is controversial. These ions function as a "buffer" to sustain the alkaline condition[29] and also participate in alkali-recycling by releasing alkalis back to the pore solution for subsequent attack.[18] Ca^{2+} incorporation in ASR gel can also form a dense semipermeable C-S-H rim around the aggregates, facilitating OH^- ion penetration into the reactive silica grain while impeding the viscous alkali silicate diffusion from the reactive site.[30] This difference in outward and inward diffusion generates an expansive force on the interfacial transition zone (ITZ), which may induce cracks.[31,32]

Increasing Al content is beneficial in mitigating ASR as it alters the crystalline ASR products into zeolite.[33] In high-Al mortar systems, ASR is inhibited by the free Si consumption, and initially forms aluminosilicate, which later transforms into a dense, impermeable zeolite-like shell ($Na_2O.Al_2O_3.5SiO_2.5.4H_2O$) and prevents alkali penetration.[32,34] Additionally, Al crosslinks alkali–silica gel layers, limiting water uptake[25] and preventing silica gel swelling.[35] Viable alternatives for introducing Al in ASR mitigation include incorporating Al-rich SCMs like metakaolin, fly ash, etc., or fine lightweight aggregates.[17,36] The decrease in Ca and increase in Al and Si by alumina-rich SCM addition result in the formation of N-A-S-H gel, which can crystallize under normal (long-term) or aggressive conditions[16] and can form zeolites with an Al/Si ratio ranging from 0.17 to 0.3.[17] The formation of zeolite-type C-A-S-H phase was also reported in limestone calcined clay cement (LC^3), effectively mitigating ASR expansion.[37] Fine lightweight aggregates (FLWAs), such as expanded slate, shale, and clay, lower alkalinity and increase alumina in the pore solution, causing the precipitation of reaction products in their pores that are more similar to C-A-S-H than alkali–silica reaction products; similar results were

TABLE 1 Chemical composition (mass%) of the raw binder materials and reactive aggregate.

	Raw material	Al_2O_3	SiO_2	CaO	Fe_2O_3	Na_2O	MgO	SO_3	K_2O	LOI
Binder materials	Kaolin	41.1	55.5	0.3	1	×	0.1	0.1	0.2	14.3
	Montmorillonite	18.7	68.4	1.5	4.3	3.1	2.4	0.9	0.4	16.4
	OPC	3.9	21.2	65.3	3.1	×	0.8	4.3	0.7	4.5
Reactive aggregate	Borosilicate	1.6	88.1	3.8	0.1	5.3	×	×	×	
	Pumice	12.5	76.0	1.3	1.4	2.5	0.9	×	5.0	

TABLE 2 Mix design.

Mixes	Aggregate type (wt%)	Binder content			Water	Fine aggregate
RRC (BS)	Borosilicate	Calcined Kaolin (56.25 g)	Calcined Montmorillonite (18.75 g)	Lime (25 g)	47 g	225 g
RRC (BS+P)	50% Borosilicate +50% Pumice					
OPC (BS)	Borosilicate	OPC (100 g)				

observed for both accelerated mortar bar test (AMBT), concrete prism test (CPT).[36,38,39]

3 | MATERIALS AND EXPERIMENTAL METHODS

3.1 | Materials and sample preparation

Recreated Roman cement (RRC) mimics the cementation process of ancient Roman concrete and is produced by combining calcined clay and hydrated lime with artificial seawater.[11] Artificial seawater was prepared as per the standard ASTM D 1141; its chemical composition is shown in Table S1. Earlier researches show that RRC exhibits better mechanical properties with a calcined clay mixture of 75% kaolinite and 25% montmorillonite, and a 75:25 ratio of calcined clay blend to lime.[10,11] In this study, RRC binders were prepared in accordance with the findings above. Pure kaolinite and montmorillonite clay, with a chemical composition shown in Table 1, and mineral composition shown in Figure 1A,B, were commercially purchased from VWR to prepare the clay blends. The clay blend calcination temperature was set at 750°C, with a heating rate of 4°C/min, a dwelling time of 6 h, and a cooling rate of 4°C/min to ensure full amorphization of kaolinite and partial amorphization of montmorillonite (Figure 1A,B).[11] The specific surface areas for the calcined kaolinite and montmorillonite were determined to be 20 and 44 m^2/g, respectively. The surface area was determined using dynamic vapor sorption tests (DVS) with commercially available DVS equipment from TA Instruments (Q5000). The water/binder ratio and sand/binder ratio of the mortar mixes were 0.47 and 2.25, respectively, according to ASTM C1260.[40] Seawater was employed as the mixing water; the mix design is depicted in Table 2. Two types of reactive aggregates, pumice and borosilicate, were used, having a chemical composition shown in Table 1. Both of the reactive aggregates were observed to be fully amorphous in nature (Figure 1C). The chemical composition of the raw materials was determined using X-ray fluorescence (XRF) (Table 1). Notably, the Na_2O equivalent of the lime-calcined clay binder, calculated according to ASTM C150, was 0.92% by mass of the binder. The particle size of pumice and borosilicate was adjusted according to ASTM C1260.[40] Moreover, for comparison, a set of OPC mortar bars with borosilicate was prepared (Table 2).

Mortar bars measuring 25 mm × 25 mm × 250 mm were prepared for mortar bar expansion measurement for 2 years. Subsequent analysis involved extracting 25 mm mortar cubes from these bars to determine their compressive strength and microstructural analysis after 2 years. Additionally, 25 mm mortar cubes were also prepared separately and cured in NaOH to determine the compressive strength after 28 days.

3.2 | Experimental methods

The accelerated mortar bar test was conducted according to ASTM C1260.[40] After demolding, initial measurements were recorded before immersing the specimens in water at 80°C for 24 h, with subsequent zero readings at room temperature. The mortar bars were immersed in a sealed plastic container with a 1N NaOH solution and kept in an oven at 80 ± 1°C for 14 days, with regular measurements of length change during this period. Afterwards, the containers with the mortar samples were taken out of the oven and kept at room temperature, where readings were peri-

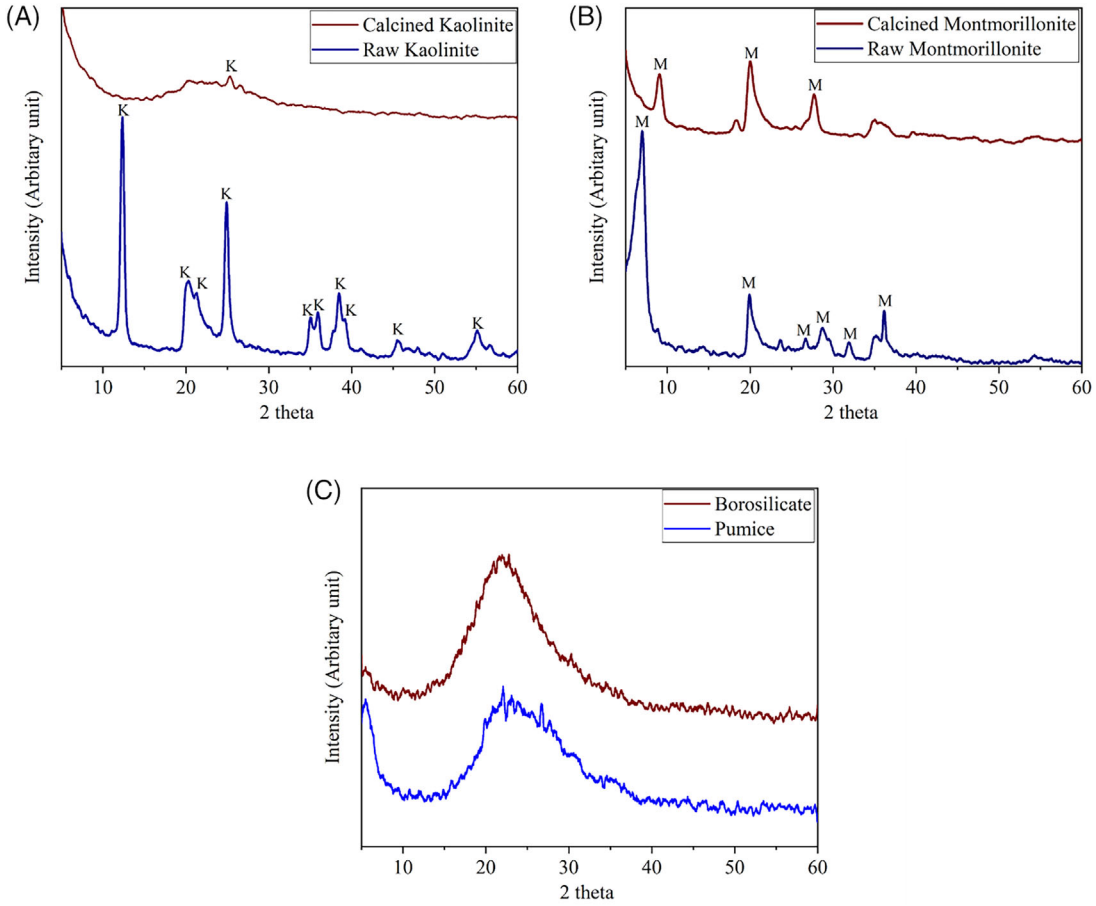

FIGURE 1 Mineral composition of (A) kaolinite, (B) montmorillonite, and (C) raw reactive aggregate. (K = Kaolinite (PDF-96-155-0599), M = Montmorillonite (PDF-96-901-0957)).

odically taken over 2 years to monitor the long-term mortar expansion. The compressive strength test followed ASTM C109.[41]

X-ray diffraction (XRD) analysis was performed to observe mineralogical changes in mortar samples over 14 days under accelerated conditions and after 2 years of alkali exposure at room temperature. A Bruker D-8 spectrometer was used at 40 kV and 40 mA with Cu Kα radiation, scanning the 2θ range of 5° to 60° at 0.03 steps per second. Mortar samples, including aggregates and pastes, were dried at 40°C, pulverized into fine powder, and sieved through a 75 μm sieve.

The evolution of silica polymerization in the RRC binder matrix was assessed using Fourier-transform infrared (FTIR) spectroscopy. Ground paste samples were analyzed in the attenuated total reflection (ATR) mode, with a resolution of 4 cm^{-1}, and 32 scans were conducted for each sample. FTIR analysis was performed on samples obtained after 7 days and 14 days of alkaline exposure to observe silica polymerization in the early stages of the reaction, as well as after 2 years to evaluate the final condition.

Scanning electron microscopy (SEM) and energy dispersive X-ray spectrometer (EDS) analysis were conducted using a HITACHI 3000N SEM operating at 25–30 kV acceleration voltage to track the progress of ASR product formation at the initial phase (7 days and 14 days) and later age (6 months and 2 years). For backscattered electron (BSE) analysis, samples containing both the peripheral and interior regions of the mortar cross-section were chosen. Point analysis, area mapping, and line scanning were used to confirm the elemental distribution of ASR products. The morphology of the ASR products was explored by secondary electron (SE) imaging.

The X-ray micro-computed tomography (microCT) test was designed to observe the cracks and internal voids along the cross-section of mortar samples containing reactive aggregates, which were exposed to alkaline conditions for two years. The experiment used a high-resolution μCT 45 (Scanco Medical, Brüttisellen, Switzerland) at a resolution of 48 μm, indicating that the pixel size detected during the analysis was greater than 48 μm. X-rays were emitted at 55 kVp and 145 μA. Mortar cubes of 25 × 25 × 25 mm^3 were scanned, producing TIFF images with 593 to

631 slices. These TIFF images were stacked using the Object Research System (ORS) Dragonfly Pro software to reconstruct 3D grayscale images.[42] First, a random slice from the XY plane of each sample was selected, and a median filter was applied to reduce image noise. Segmentation was then performed to separate the voids and aggregates from the binder matrix. The process for the segmentation is as follows:

- Defining a region of interest (ROI) that included both external and internal void spaces and a second ROI that encompassed the solid portions along with the internal voids. The intersection of these two ROIs yielded the final ROI for the voids within the solid object.
- Defining the ROI for aggregates by selecting the grayscale range specific to borosilicates.
- Generating the final image by combining the smoothed grayscale image with the ROIs for internal voids and aggregates.

4 | EXPERIMENTAL RESULTS

4.1 | ASR-induced expansion

Figure 2A shows the RRC and OPC mortar bars' expansion caused by the formation of hydrophilic ASR gel to evaluate their durability against alkaline exposure.[43] When measured according to ASTM C1260, the mortar bar expansion more than 0.1% at 14 days indicate potentially reactive aggregate.[40] Considering borosilicate is highly susceptible to ASR, the expansion of OPC mortar bars containing borosilicate aggregate reached the 0.1% limit within 6 days, and by 14 days, it was around 0.2%. Previous literature reported calcium as the primary reason for this high ASR-induced expansion in OPC concrete, as it increases gel viscosity and yield strength.[18] This high-viscosity gel causes internal swelling and eventually cracks the matrix.[44] However, after 14 days, RRC (BS+P) and RRC (BS) reached only 0.007% and −0.002%, respectively, which is significantly below the limit and nearly negligible.

To evaluate the long-term behavior of the novel RRC binder under alkaline exposure, the sample's expansion was monitored for up to 2 years. Nevertheless, even after 2 years, the maximum expansion reached by RRC mortar bars was only 0.02% (Figure 2B). The slight downward trend of length expansion observed after 2 years of exposure could be attributed to chemical shrinkage resulting from geopolymerization,[45] as previous literature has confirmed the coexistence of both C-A-S-H and geopolymer gel in the lime-calcined clay binder microstructure.[10,11] Long-term exposure to alkali had a minimal impact on the compressive strength of the RRC (BS+P) sample; after 2 years, the strength remained within the standard deviation of the strength measured at 28 days (Figure 2C). In contrast, the RRC (BS) sample imparted only a 3 MPa compressive strength reduction after 2 years. Notably, the RRC (BS+P) sample exhibited around 52% higher compressive strength than the RRC (BS) sample. To understand the low expansion in these mortar bars, detailed microstructural evaluations were performed, and further discussion is provided in the subsequent sections.

4.2 | Evolution of phase formation during long-term alkali exposure

Both RRC (BS) and RRC (BS+P) samples remained highly amorphous after 14 days of alkaline exposure at elevated temperatures (Figure 3A,B). Notably, the montmorillonite dissolution was incomplete at this stage, and the primary reaction products formed were ettringite, hydrocalumite, gismondine, and gehlenite, with RRC (BS+P) also forming stratlingite. Ettringite and hydrocalumite formation were due to using seawater as the mixing water. Early studies of this seawater-mixed lime-clay binder also revealed the formation of these phases.[10] Moreover, the presence of an aluminosilicate phase, gismondine, was evident in both the lime-clay mortar samples after 7 days and 14 days of exposure (Figure 3A,B). Zeolite-like gismondine formation was observed in a previous study during the pozzolanic reaction between metakaolinite and $Ca(OH)_2$ at 60°C over extended hydration periods.[46]

However, after 2 years, the calcium-bearing minerals that formed in the early stages (at 7 and 14 days), such as ettringite, hydrocalumite, gismondine, and gehlenite, had disappeared, with several crystalline zeolites, including phillipsite and chabazite, emerging as dominant phases in both RRC samples (Figure 3A,B; 2 years). Mineralogical analysis of the reactive aggregates confirmed them to be entirely amorphous (Figure 1C), indicating that the zeolite phases did not originate from the raw aggregates. Instead, these phases were stabilized by the abundant Al present in the calcined clay and pumice (Table 1).[47,48] As in Roman concrete, high alumina content promoted Al^{3+} substitution for Si^{4+} in Q^3 tetrahedral sites, supporting [Al^{3+} + Na^+] substitution and potential for cation exchange.[5] The FTIR spectra of the RRC binder matrix also confirm the increased silica polymerization after 2 years (Figure 4). It was observed that initially (7 and 14 days), distinct peaks at 960 cm^{-1} (Q^2) and a shoulder at 1023 cm^{-1} (Q^3) indicated the formation of C–A–S–H and geopolymer gels.[49,50] After 2 years, these peaks merged into a sharper band at 980 cm^{-1}, with reduced width, reflecting enhanced Si-O-T polymerization.[51] The Ca-bearing minerals formed ini-

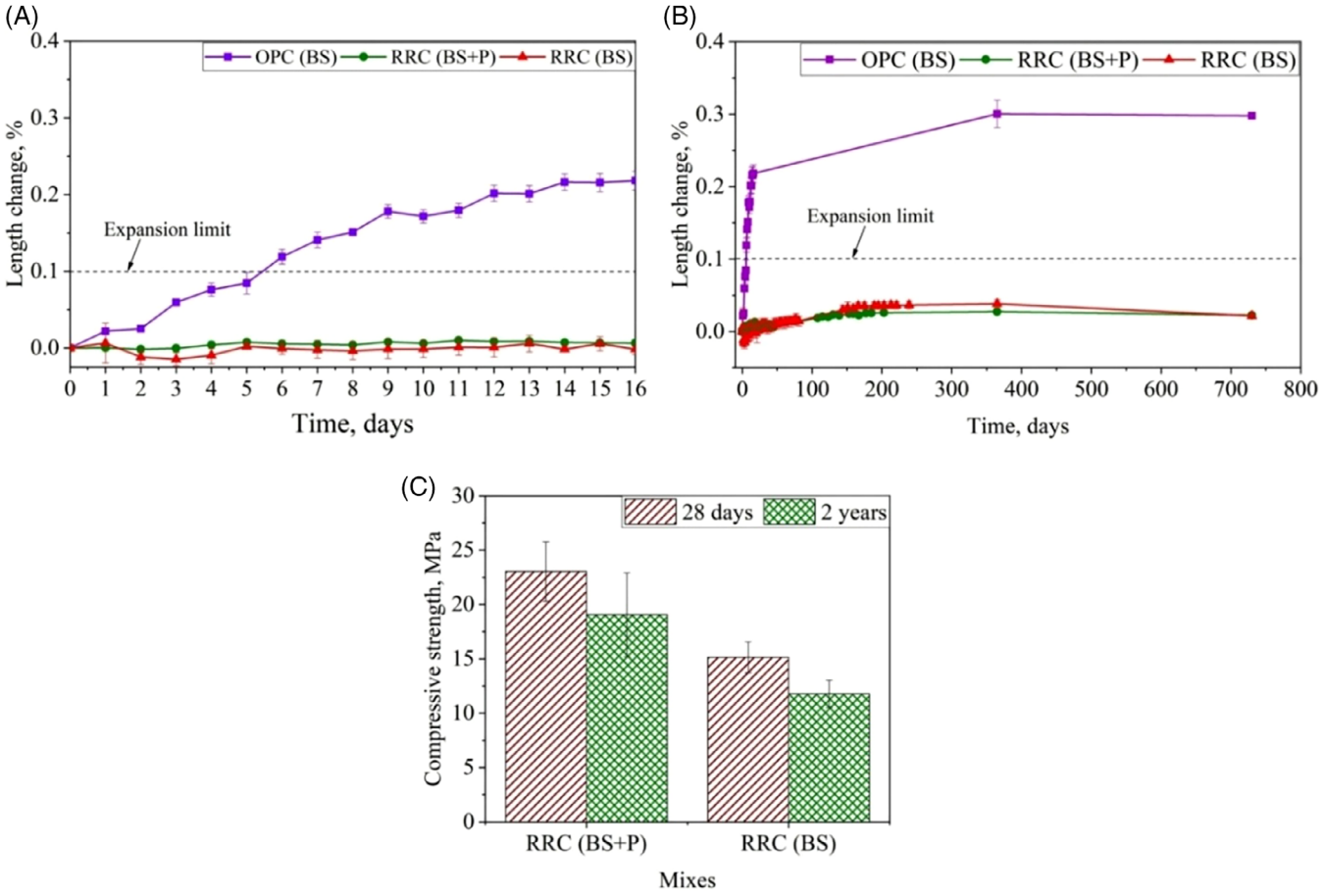

FIGURE 2 ASR-induced expansion up to (A) 16 days, (B) 2 years, and (C) compressive strength of RRC mortar.

tially in the RRC system (Figure 3A,B; 7 days and 14 days), being the only Ca-containing phases once portlandite was depleted, likely decomposed to provide Ca for contributing to this cation exchange process. In addition to the zeolite phases, the RRC (BS+P) sample, the presence of shlykovite ($CaH_7kO_{13}Si_4$) was identified at 2θ values 6.65° and 13.1° in the RRC (BS+P). K-shlykovite ($KCaSi_4O_8(OH)_3{\cdot}2H_2O$) and Na-shlykovite ($NaCaSi_4O_8(OH)_3{\cdot}2.3H_2O$) are two laboratory-synthesized layered silicate sheet structures resembling the ASR products formed in the field;[52] these minerals have a similar basal spacing of 13.1 Å (7.7° 2θ) as the natural mineral shlykovite.[53,54] Exposure to high temperature (80°C) for the first 14 days,[54] or long-term alkaline exposure, instigated the crystallization of ASR product.

Due to the abundant presence of Al and Si, C-A-S-H and geopolymer gel coexist within the RRC microstructure.[55] Thereby, a sharp peak at~29° 2θ was observed in RRC samples related to the C-A-S-H phase formed in the early stage (within 7 days), which remained stable over extended exposure (2 years).[56] The RRC sample mineralogy was also compared with that of the OPC sample (Figure 3C). In OPC, a broad C-S-H peak was visible at the 29° 2θ along with several portlandite peaks at 18°, 34°, and 47° 2θ. Previous studies have confirmed that Ca presence is necessary to cause ASR expansion.[53,57] However, none of the RRC samples exhibited portlandite remaining, thus indicating its potential in mitigating ASR expansion.

4.3 | Morphology of the ASR products

The morphologies of the ASR products developed in different matrices are illustrated in Figure 5. In both RRC (BS+P) (Figure 5A) and RRC (BS) (Figure 5D) samples, a few plate-like structures were observed, surrounded by minerals exhibiting prism-like morphologies. Upon exposure to NaOH solution, crystalline ASR product known as Na-shlykovite, characterized by plate-like morphology with isometric dimensions, can form in mortar with reactive aggregate.[52,58,59] These minerals typically form rosette-like arrangements irrespective of concrete mixtures and binder types.[17,53] As observed in Figure 5C,F, both RRC samples showed the presence of shlykovites, confirmed by point EDS analysis; however, the rosette-like

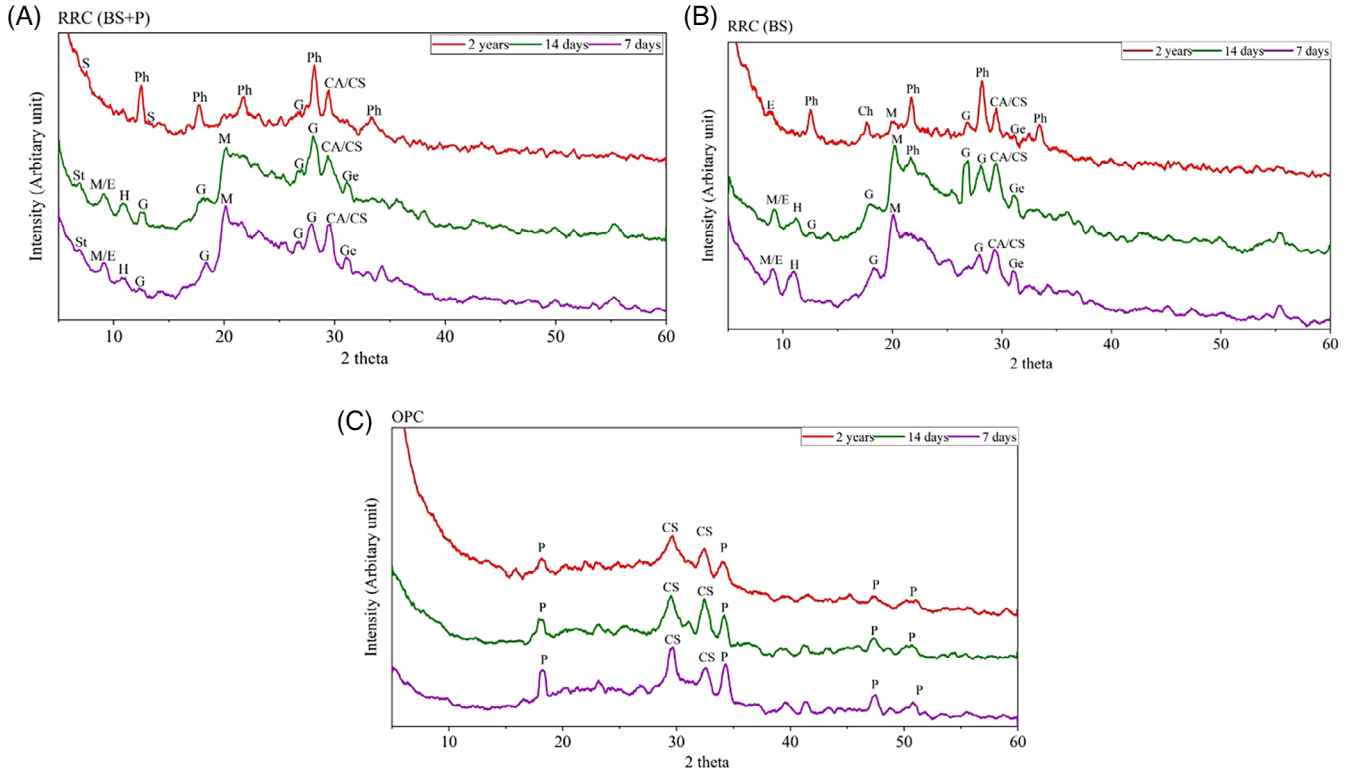

FIGURE 3 Mineralogical evolution over 2 years of alkali exposure: (A) RRC (BS+P), (B) RRC (BS), and (C) OPC (BS). (S = Shlykovite-PDF-96-901-6221, E = Ettringite-PDF-96-901-2923, H = Hydrocalumite-PDF-96-900-9354, Ph = Phillipsite-PDF-96-901-3302, Ch = Chabazite-Ca-PDF-96-900-9307, CS = C-S-H, CA = C-A-S-H, P = Portlandite-PDF-96-100-1769, G = Gismondine-PDF-96-901-0502, Ge = Gehlenite-PDF-96-900-4072, St = Stratlingite-PDF-96-900-5060, M = Montmorillonite-PDF-96-901-0957).

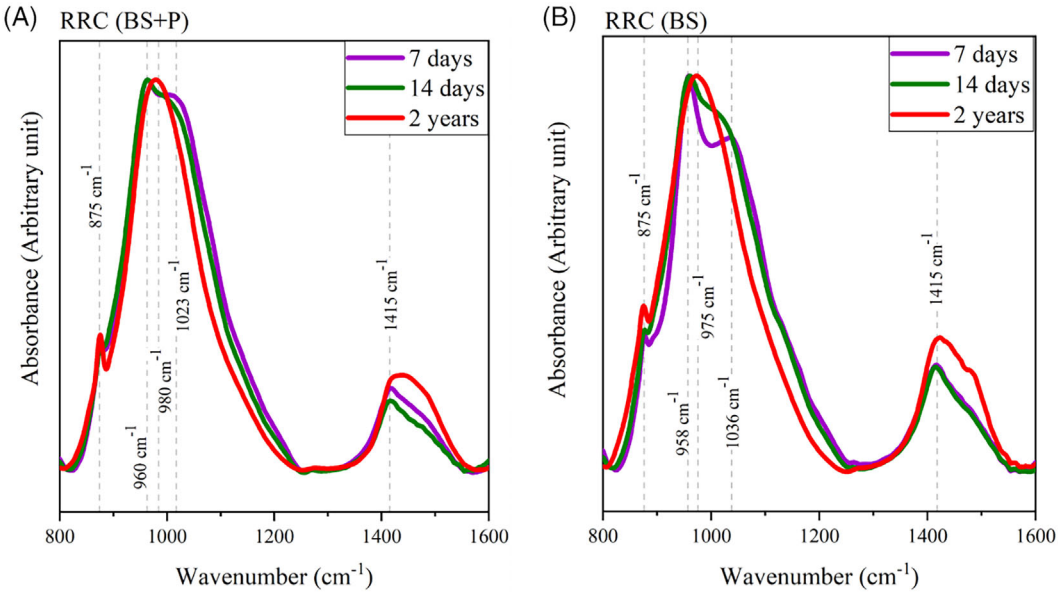

FIGURE 4 Evolution of silica polymerization over 2 years of alkali exposure: (A) RRC (BS+P), (B) RRC (BS).

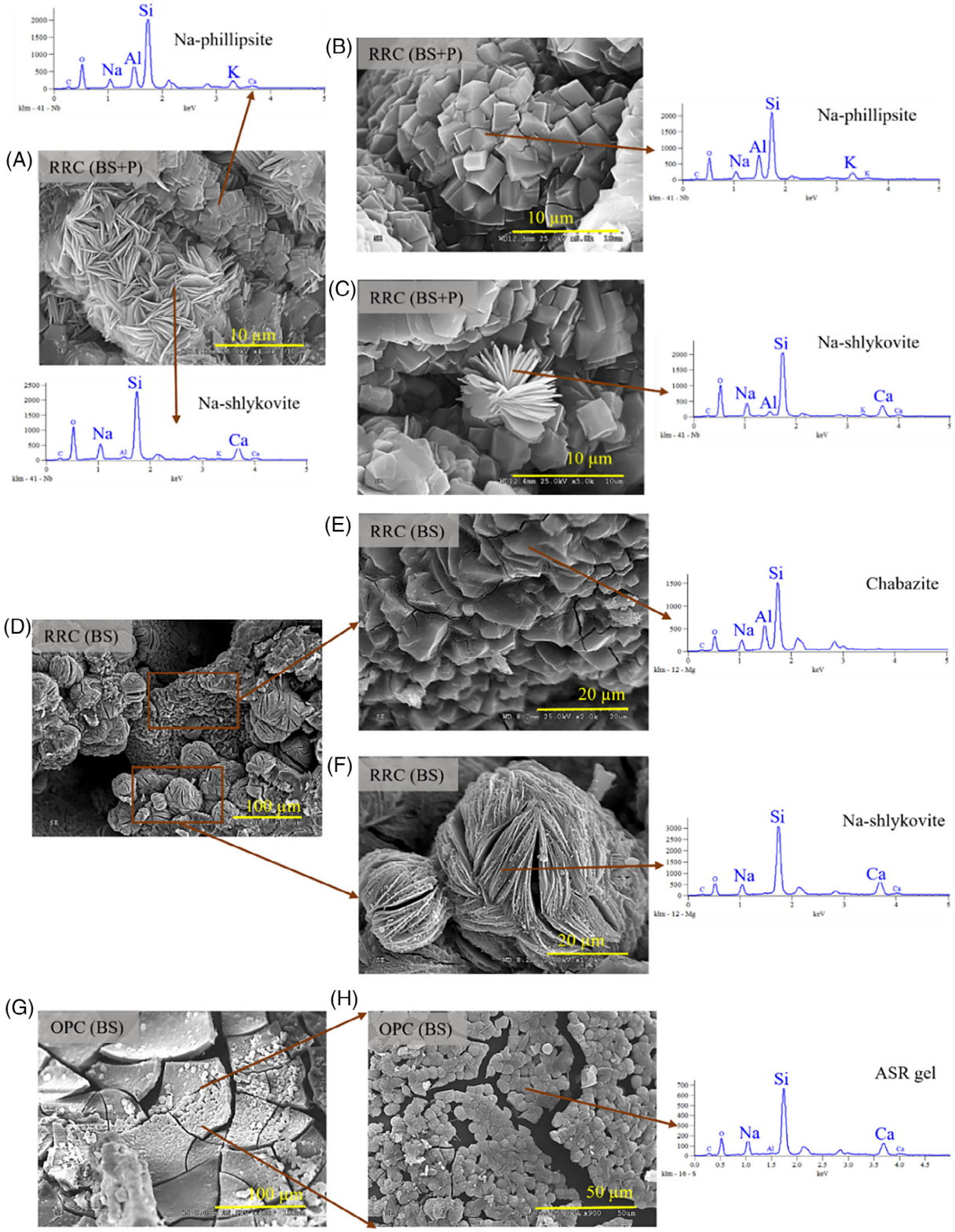

FIGURE 5 Morphology of (A) co-existing ASR crystals and zeolite, (B) zeolite, (C) Na-Shlykovite in RRC-pumice sample, and (D) co-existing ASR crystals and zeolite, (E) chabazite, (F) Na-Shlykovite in RRC-borosilicate sample. (G, H) Morphology of the ASR product formed in the OPC-borosilicate sample.

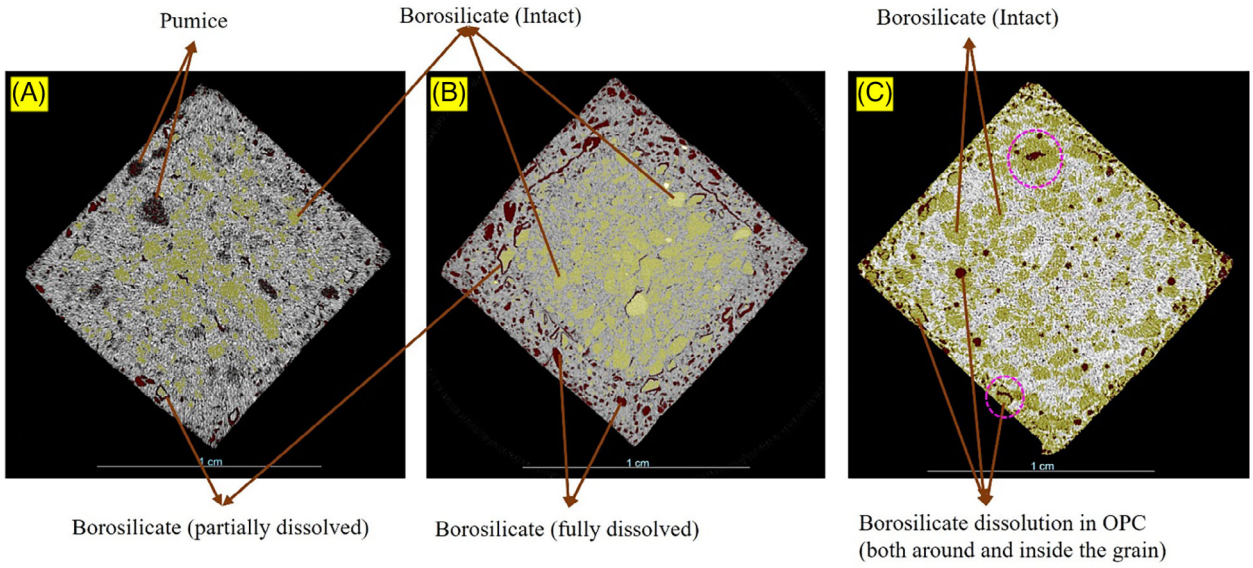

FIGURE 6 Cross-section of (A) RRC (BS+P), (B) RRC (BS), (C) OPC (BS), obtained by microCT analysis. Reddish brown: voids and cracks, yellow-brown: borosilicate, grey: binder matrix.

arrangement of these minerals differed between the RRC mixes. In RRC (BS+P), the plate-like minerals formed a flowery pattern, connecting to a single point at the cluster's bottom and spreading toward the top (Figure 5C). In contrast, in the RRC (BS), the plates were densely packed (Figure 5F). Additionally, the prism-shaped morphology surrounding the crystalline ASR products was identified as zeolites as per the EDS analysis (Figure 5A,D). In RRC (BS+P), a prismatic Na-phillipsite cluster was observed (Figure 5B); however, the zeolite morphology observed in the RRC (BS) closely matched chabazite, as also identified by the XRD analysis of this sample. A similar phenomenon was observed in pumice vesicles within ancient Roman concrete, where zeolites like phillipsite and chabazite were discovered filling these voids, ultimately consolidating the ITZ of pumice clasts.[5,60] The ASR product morphology observed in the OPC sample closely resembled nanocrystalline ASR gel (Figure 5G,H).[52]

4.4 | Cross-section observation using microCT analysis

Figure 6 shows the cross-sections of the samples, where the internal voids are represented in reddish-brown, the borosilicates in yellow-brown, and the binder matrix in light grey. In RRC (BS+P), the large dark grey areas represent pumice, which appears darker than the binder matrix due to its internal pores (Figure 6A). The RRC sample containing both pumice and borosilicate exhibited a dense microstructure without any crack formation (Figure 6A). Only a few borosilicates at the peripheral region were partially dissolved, suggesting that pumice incorporation may help to prevent borosilicate dissolution. Conversely, in the RRC (BS) sample, the reddish-brown area (Figure 6B) showed a prominent and homogeneous presence of completely or partially dissolved borosilicates, indicating significant alkali impact in this region. Notably, the core region of this sample remained dense without any signs of aggregate dissolution. However, crack formation was observed along the interface between the peripheral region and the dense core in the RRC (BS) sample (Figure 6B). In the OPC sample with borosilicate, the reddish-brown zones were observed not only in the peripheral region of the sample but also throughout its core zone (Figure 6C). As opposed to RRC (BS), complete leaching of borosilicate was not observed in OPC (BS), suggesting these dissolved aggregates likely remain embedded within the binder matrix. Moreover, aggregate dissolution was observed within the borosilicate grains, highlighted by the reddish-brown areas inside the irregular yellow-brown regions (Figure 6C).

4.5 | Evaluation of ASR product formation mechanism by SEM analysis

MicroCT analysis (Figure 6) revealed that aggregates in the peripheral region of the RRC samples were primarily affected by alkali, as evidenced by the voids left from their dissolution. Therefore, SEM-BSE analysis was performed on samples taken from the peripheral region of the mortar bars.

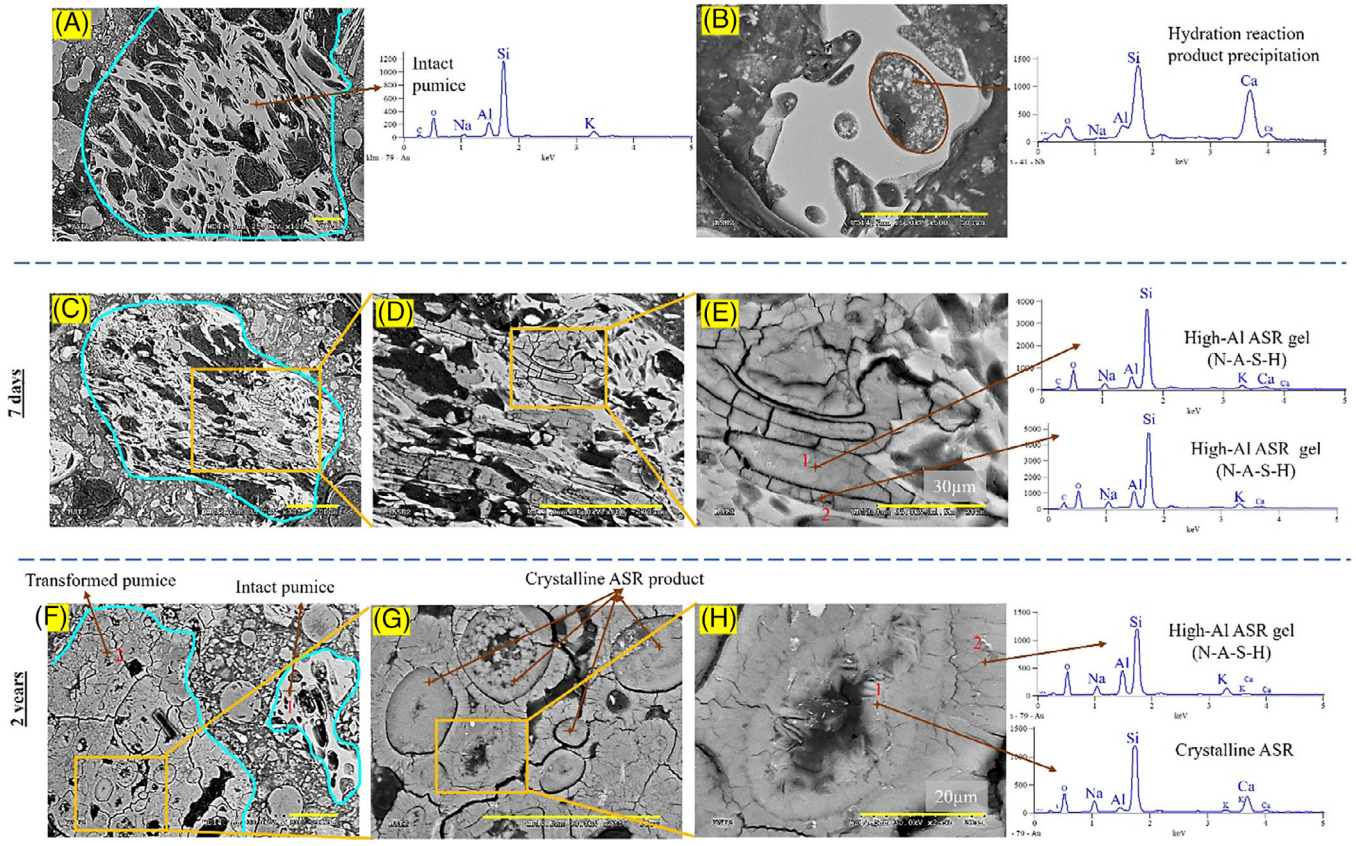

FIGURE 7 BSE images representing the alkali–silica reaction progress in pumice within the lime-clay matrix: (A) intact pumice, (B) hydration product in pumice void, N-A-S-H gel forming from initial aggregate dissolution after 7 days, (F–H) crystalline ASR at the core of high-Al ASR gel in fully transformed pumice after 2 years. The Y-axis of the EDS spectrum indicates atomic%. The yellow bars in images (A–D) and (F, G) indicate a 100 µm scale.

4.5.1 | ASR effect on pumice aggregate in a lime-calcined clay matrix

ASR product formation mechanism

BSE image analysis was conducted on the alkali-exposed pumice aggregate embedded in the lime-calcined clay matrix at 7 days (early age) and 2 years (long-term). Figure 7A depicts an intact pumice with visible internal voids, some of which are filled with a C-A-S-H-like gel precipitate—one of the binder's hydration products (Figure 7B). This way, lightweight aggregates mitigate ASR by absorbing alkalinity from the pore solution within their internal voids.[38,39] The alkaline pore solutions likely began dissolving the aggregate internally, producing a sodium aluminosilicate (N-A-S-H) gel phase containing silicon (Si), aluminum (Al), and sodium (Na) as the ASR product, which filled the voids in the partially dissolved pumice within 7 days of alkaline exposure (Figure 7C,D,E). The magnified image in Figure 7E reveals a gradual separation between the two phases. Although EDS analysis shows both as N-A-S-H gel, the inner product (Figure 7E, point_1) exhibits a smoother morphology than the outer product (Figure 7E, point_2). This ASR product is referred to as "high-Al ASR gel" due to its high incorporation of Al ions. Long-term (2 years) alkali exposure increased the gel phase quantity gradually, disintegrating the unreacted aggregate (Figure 7F). Therefore, coexisting undissolved pumice with a relatively smooth surface (Figure 7F, point_1) and the reaction product formed from the dissolved pumice were observed (Figure 7F, point_2). Notably, the reaction product remains at its formation site, indicating its stability (Figure 7F,G). Eventually, the entire pumice was observed to transform into an ASR product with a composition of Si, Al, and Na (high-Al ASR gel) (Figure 7H, point_2), and a crystalline morphology at its core (Figure 7H, point_1). EDS analysis confirms that this phase at the core is composed of Ca, Na, and Si, resembling the composition of ASR crystal.[22] SEM images (Figure 5) and XRD (Figure 3) confirm zeolites and crystalline ASR phase formation in the RRC binder matrix. ASR phases were not observed in the initial alkali exposure at elevated temperature (Figure 7C,D,E). Therefore, their crystallinity

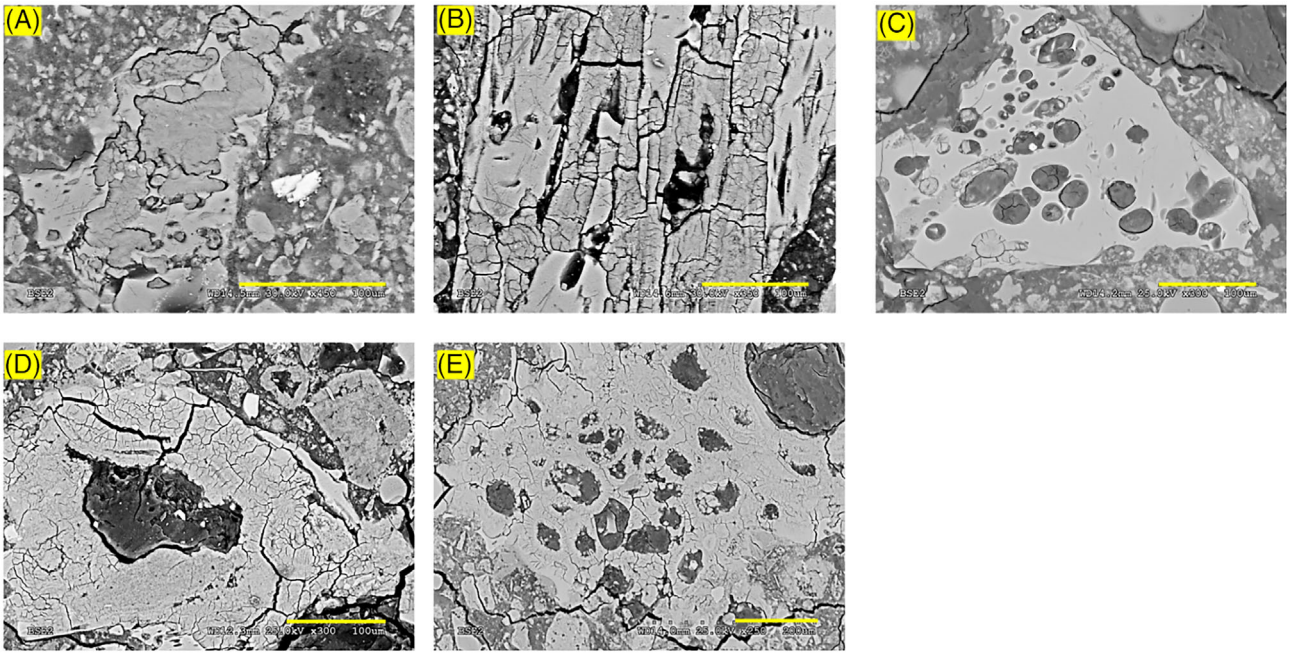

FIGURE 8 (A–E) Pumice dissolution in RRC mortar, showing uniform conversion of the aggregate into ASR products throughout the sample. The yellow bars indicate a 100 μm scale.

has originated from long-term alkaline exposure.[54] Similar observations were made throughout the RRC (BS+P) sample, confirming the representativeness of the findings (Figures 8 and 9).

Composition of ASR products

The BSE image in Figure 10A illustrates the final products formed in the pumice void due to their alkaline susceptibility, and Figure 10B depicts the gradual elemental variations monitored through the EDS line scan. The BSE image reveals three distinct phase formations arranged from right to left: a smooth surface, a textured structure, and a product cluster exhibiting a crystalline texture. The smooth surface represents the unreacted pumice, primarily composed of Si and Al, maintaining a consistent Si/Al~8. However, a gradual increase in Al and Na, along with a decrease in Si and absence of Ca, was observed toward the phase on the right side of the pumice surface. This phase exhibited an Si/Al = 5~6. The crystalline cluster next to this phase exhibited a rise in Ca, with complete exclusion of Al, while the diminution of Si and the increase of Na continued. Proceeding further, the elemental composition again changed by increasing Al and decreasing Ca.

The distinction among the reaction products was also evident from the area mapping (Figure 10C). The mapping unveils a dense Ca concentration within the core region and a substantial presence of Al in the surrounding zone. The crystallization of both ASR products, the outer high-Al ASR phase and the Ca-bearing ASR phase at its core, was confirmed by the presence of the zeolitic phase, phillipsite, surrounding the crystalline ASR product, as observed in the ASR morphology analysis (Figure 5A). The shrinkage due to crystallization caused a distinct gap in the ITZ between the unreacted pumice and zeolite, as well as between zeolite and crystalline ASR (Figure 10A,C). However, there was no evidence of expansion cracks causing fractures in the aggregate due to their formation or crystallization, as the reaction products formed within the aggregate void.

4.5.2 | ASR effect on borosilicate aggregate in a lime-calcined clay matrix

ASR product formation mechanism

As per the microCT analysis, borosilicate damage or dissolution was highly pronounced in the peripheral region of the RRC (BS) sample, while the core remained largely unaffected (Figure 6B). Therefore, BSE analysis of this sample was performed after 7 days, 6 months, and 2 years of alkaline exposure, focusing mostly on the peripheral region (Figure 11). Fully or partially dissolved borosilicate distribution in the RRC (BS) matrix is shown in Figure 12A. Arranging images of dissolved aggregates at varying degrees, along with corresponding EDS, revealed a sequence of reaction product formation. Figure 11A shows a borosilicate particle, unaffected by alkali, embedded within the lime-calcined clay matrix. Upon alkali attack, the reaction initiated at the aggregate-binder inter-

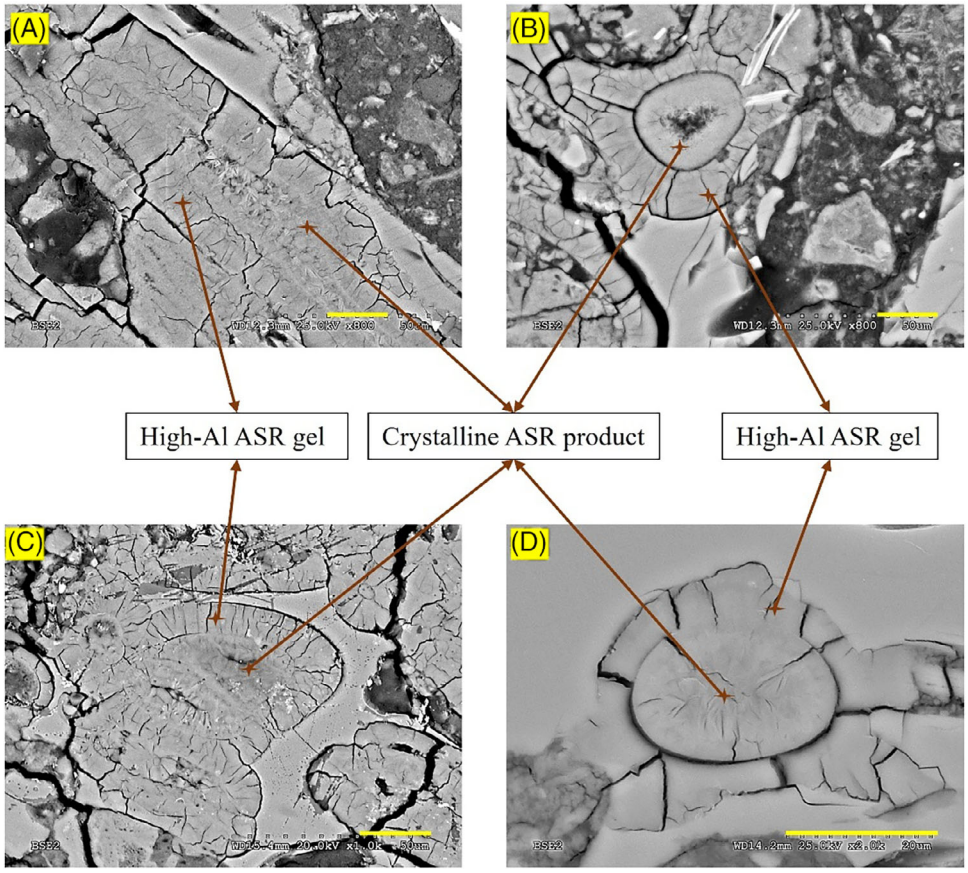

FIGURE 9 (A–D) Co-existence of high-Al ASR gel and crystalline ASR product formation from pumice dissolution in RRC mortar. The yellow bars indicate a 20 μm scale.

face (Figure 11B,C) due to the inherent reactivity of borosilicate.[18] At 7 days, the peripheral region of the aggregate appeared empty, indicating that the reaction product from borosilicate dissolution was a low-viscosity substance that left the reaction site (Figure 11B,C). EDS analysis identified the residual product at the reaction site as a sodium silicate hydrate (N-S-H) gel (Figure 11B,C). Over the long-term exposure (up to 2 years), Al and Ca from the binder matrix were observed to incorporate into the initially formed N-S-H gel at the ITZ of aggregate and cement matrix (point_1 in Figure 11D,E). Al enhanced the crosslinking of the N-S-H gel, forming zeolite phases[61] and enhancing its stability. However, the N-S-H gel without binder contact lacked Al or Ca (Figure 11D, point_2); this gel eventually leached or dispersed within the binder matrix, indicated by the void left at the reaction site (Figure 11E). The green-colored region illustrates the reaction product extruded into the binder matrix (Figure 11F). However, in this process, large voids are left by the dissolved borosilicates (dark regions in Figure 11C,E,G). Moreover, borosilicates can also undergo an entire conversion into crystalline ASR products and stay at the reaction site (Figure 11G); notably, Al uptaking takes place at the interface region of this crystalline product, forming C-N-A-S-H. Interestingly, in RRC (BS) sample, even though varying degrees of borosilicate dissolution was observed in the peripheral region, the aggregates most remained intact in the core region of the mortar (Fig. 12

Composition of ASR products

An entire borosilicate conversion into a crystalline ASR product was identified from the BSE image. Figure 13A shows round-shaped borosilicate grains with 50–60 μm diameters alongside larger, irregularly shaped borosilicates in the matrix. The BSE image in Figure 13B presents two of those round borosilicate aggregates; the left one was predominantly occupied with untextured gel product with a crystalline formation emerging on its right side, whereas the right side aggregate was entirely filled with crystalline clusters along with the untextured gel product adhering to the boundary region. The EDS linescan in Figure 13C shows that the Si content in the line scan passing through both aggregates remained constant. Nevertheless, while the untextured zone displayed a composition resembling geopolymer, containing Ca, Si, Na, and Al, upon entering the crystalline textured zone, there was a sudden

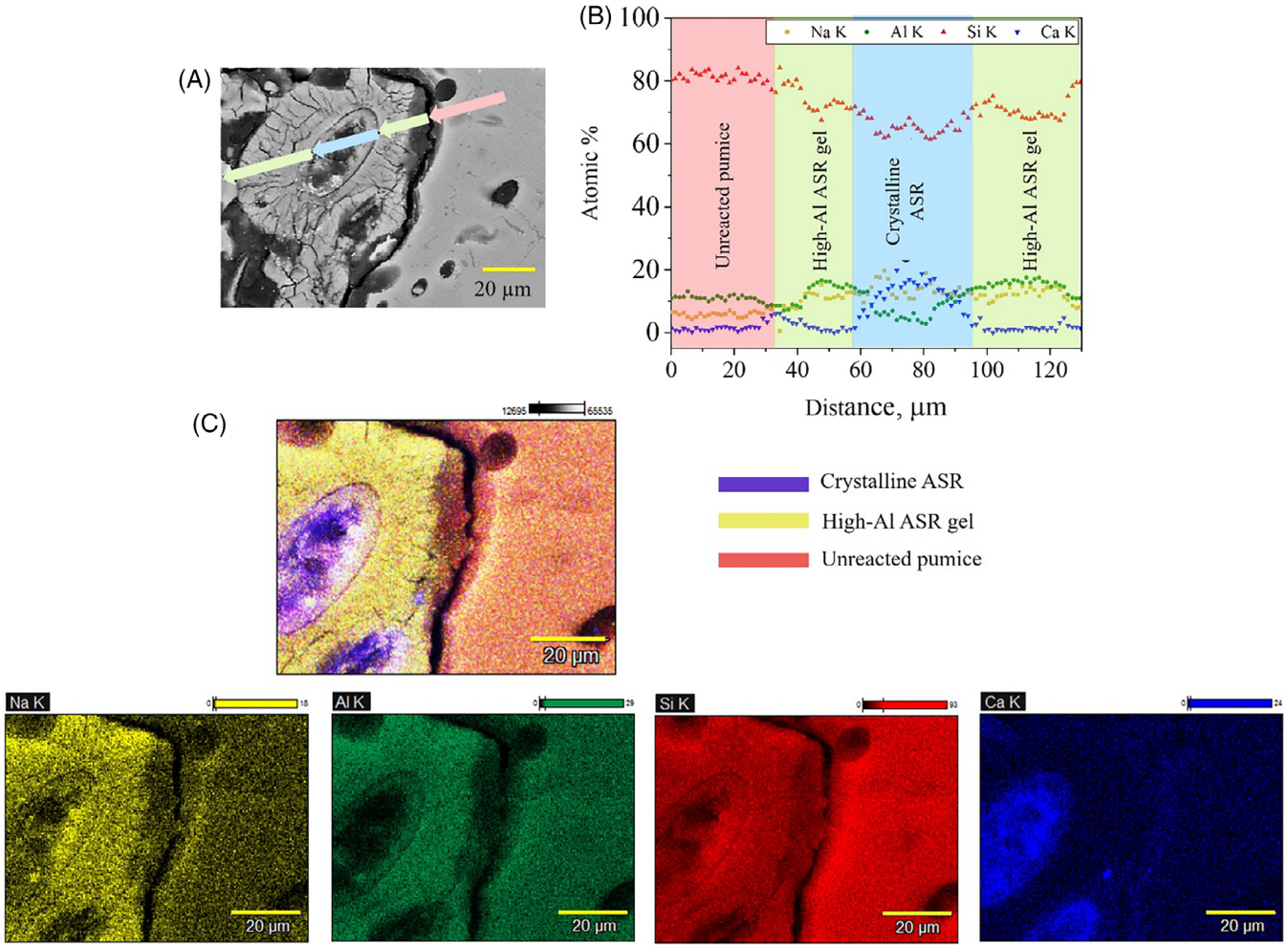

FIGURE 10 (A, B) Compositional variation, and (C) area mapping of ASR products in pumice. The yellow bar indicates a 20 µm scale.

increase in the atomic percentage of Ca, accompanied by an equivalent reduction in the atomic percentage of Al. The observations indicate that borosilicate can fully convert into the crystalline ASR product or C-N-A-S-H gel because Al and Ca continuously intrude into the aggregate, preventing dissolved silica gel from leaving the binder matrix and promoting its combination at the reaction site. As depicted in Figure 13D, the elemental area mapping validates this observation by revealing a concentrated distribution of Al in the left aggregate, primarily consisting of C-N-A-S-H gel; in contrast, the right-side aggregate with crystalline formation exhibits a dense distribution of Ca.

4.5.3 | ASR effect on borosilicate aggregate in OPC matrix

ASR product formation mechanism

The ASR mechanism within the OPC matrix has been extensively analyzed in previous studies and is now firmly established.[22,29] Therefore, only a minimal discussion is provided here for comparison purposes. The analysis was conducted on an OPC sample with borosilicate aggregate after 2 years of alkali exposure. ASR product formation was observed both at the aggregate–binder matrix interface region (Figure 14A,B) and within the aggregate itself, where dissolution initially began at the interface (Figure 14). In the OPC system, portlandite is a hydration product; therefore, abundant Ca ions are available to react with the previously formed gel products at the periphery, which is observed in (Figure 14B, point 1). However, high-Ca ASR gels are highly viscous,[44] which prevents the dissolved silica from getting out but allows OH^- ions to get in. Eventually, low-Ca ASR gel forms inside the outer ASR layer due to the absence of portlandite in the interior of the aggregate, which exerts pressure to crack the aggregate[18] and proceeds freely through the intra-aggregate microcracks. Nevertheless, the gel in the interior region lacks Ca ions because it is distant from the cement matrix (Figure 14B, point 2). These ASR gels eventually swell up and put pressure on the matrix to create cracks

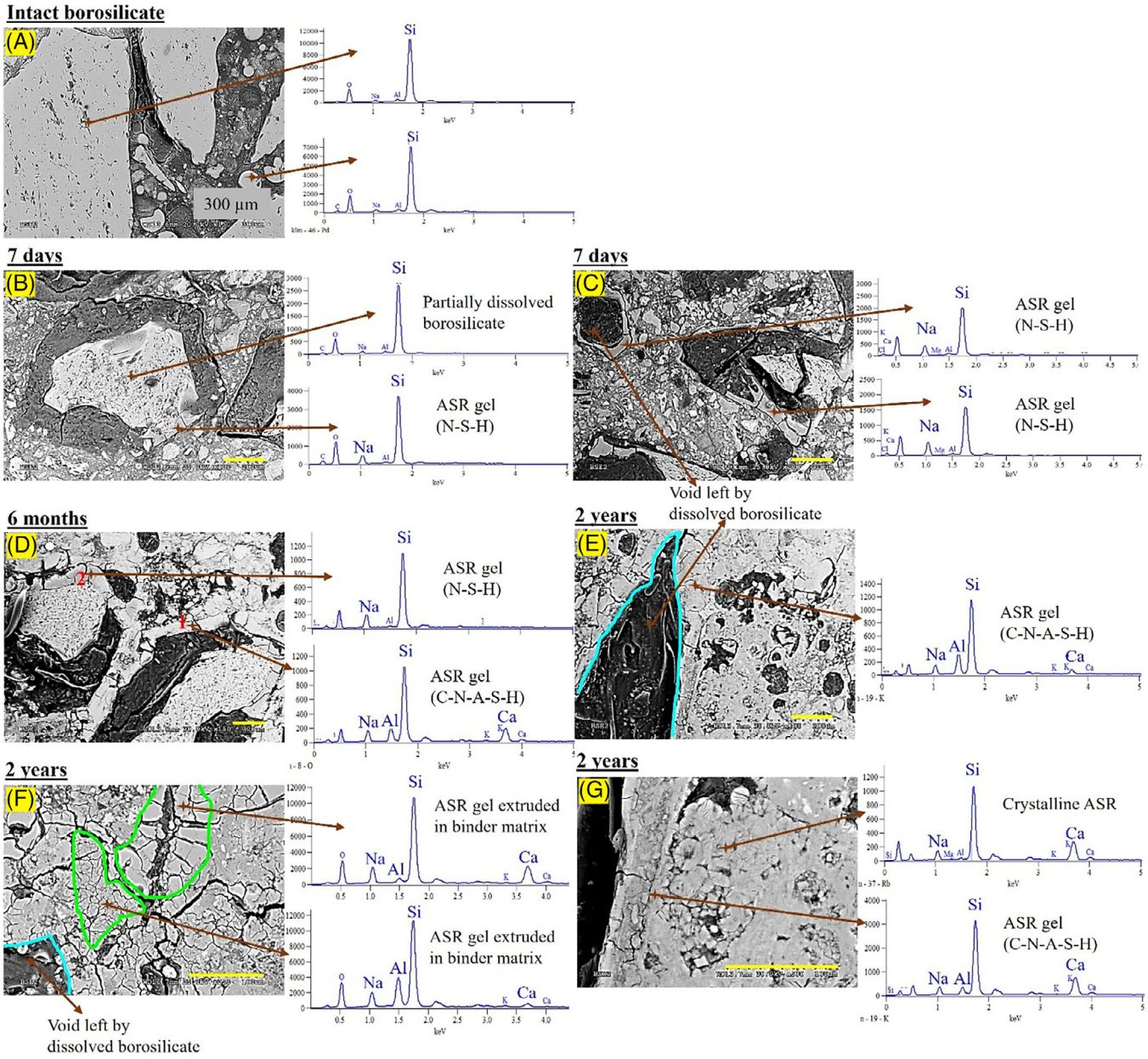

FIGURE 11 BSE images representing the progression of alkali–silica reaction in borosilicate within the lime-clay matrix over time. (A, B) Borosilicate dissolution forming N-S-H gel as the primary reaction product, (C) Al incorporation at the boundary forming C-N-A-S-H, (D) void left by fully dissolved borosilicate, (E) ASR product extrusion into binder matrix, (F) complete borosilicate conversion into crystalline ASR. The yellow bars indicate a 100 µm scale.

and get out. It was observed from Figure 14C that the gel extruded in the cement matrix has high Ca intensity, which can be attributed to the higher calcium uptake in the ASR gel. Moreover, as depicted in Figure 14D, the ASR gel in the interior region continued to bind Ca when the aggregate dissolution increased. Eventually, it formed an ASR gel with a homogeneous composition. The observations drawn from the ongoing evaluation of the OPC sample are similar to the previous studies[19]

4.6 | Elemental analysis of ASR products

Quantitative elemental analysis using BSE-EDS involved selecting approximately 100 points per sample from the alkali–silica reaction products, both amorphous and crystalline, and determining their Al/Si, Ca/Si, and (Na+K)/Si. From the plots Al/Si versus Ca/Si and (Na+K)/Si versus Ca/Si shown in Figure 15, correlations between Ca, Al, Na, and K in different ASR products can be evaluated.

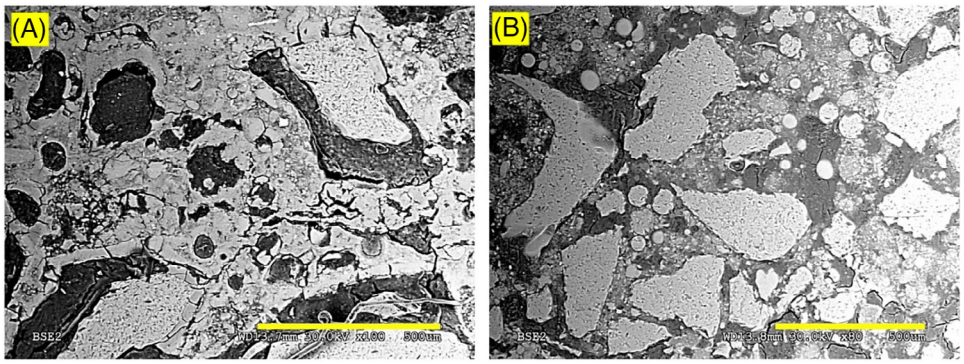

FIGURE 12 (A) Varying degrees of borosilicate dissolution at the peripheral region and (B) unaffected matrix with intact borosilicates at the mortar core. The yellow bars indicate a 500 μm scale.

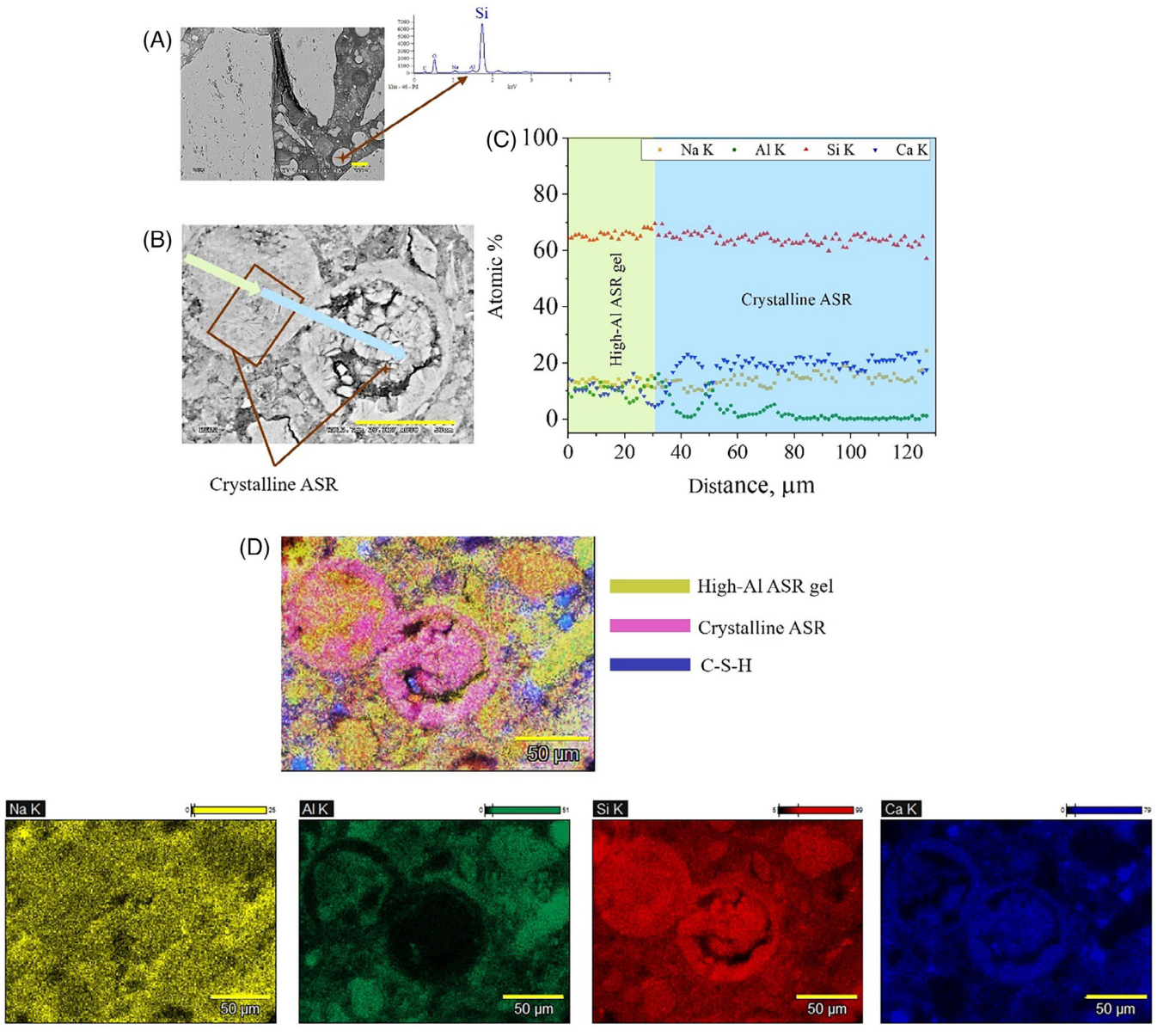

FIGURE 13 (A–C) Compositional variation and (D) area mapping of ASR products in borosilicate. The yellow bar indicates a 50 μm scale.

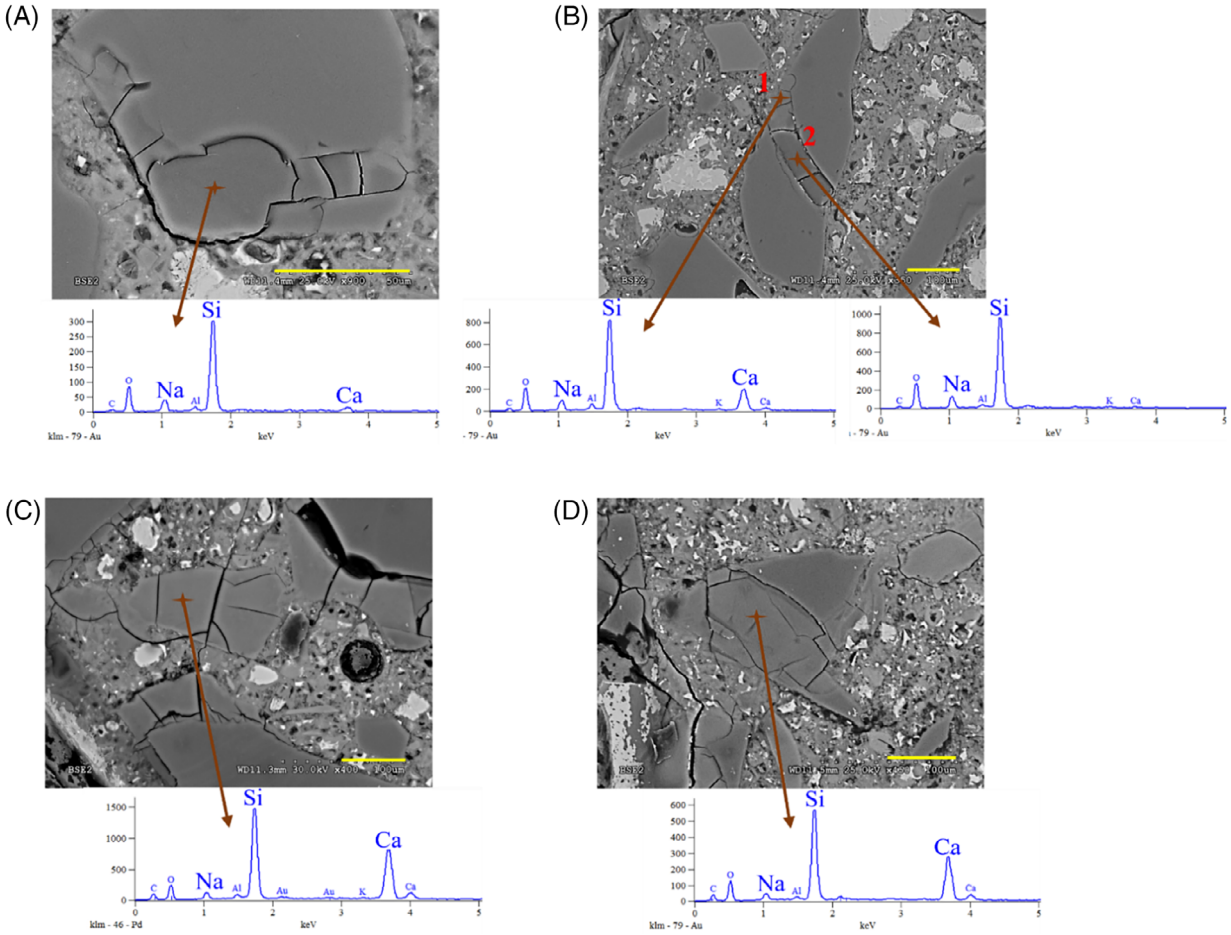

FIGURE 14 BSE images representing the alkali–silica reaction from borosilicate dissolution within the OPC matrix. The yellow bars indicate a 50 μm scale.

Duan et al.[44] state that a Ca/Si ratio below 0.1 signifies the intermediate stage of silica dissolution, later leading to the ASR product formation having a Ca/Si ratio exceeding 0.1. A Ca/Si ratio of 0.1 was established as a dividing point for categorizing EDS points. In the RRC (BS+P) sample (Figure 15A), EDS points with Ca/Si ratios below 0.1 displayed an Al/Si range of 0.2–0.3. Higher Al/Si suggests increased polymerization of free silica from the dissolved aggregate, leading to the alkaline aluminosilicate formation, which later can transform into a zeolite phase.[32] Therefore, this point cluster was identified as the high-Al ASR gel. However, in the RRC (BS) sample (Figure 15B), alongside the high-Al ASR gel cluster, a silica gel cluster was observed, possibly due to lower Al availability than in the pumice-containing sample; this silica gel may transform into ASR gel by absorbing Ca or into polymerized aluminosilicate gel by absorbing Al. Notably, both amorphous and crystalline ASR products depicted a decline in the Al/Si ratio with increasing Ca/Si ratio. Being a low calcium binder, the Ca/Si of ASR products formed in RRC ranged between 0.1 and 0.4, where the Ca/Si ratio in crystallized ASR products surpassed that in amorphous products (Figure 16A). In contrast, the ASR product in the OPC matrix showed a wide Ca/Si range of 0.1–0.9 due to the presence of $Ca(OH)_2$ as a hydration product (Figure 15C); moreover, the Al/Si of these points was negligible. As shown in Figure 14, in OPC, ASR products extruded to the binder matrix had higher Ca/Si relative to the gel formed within the aggregate, as they could uptake Ca ions from the matrix. This phenomenon justifies the wide Ca/Si ratio variation range of ASR products in the OPC (Figure 15C); near the aggregate, this value can be around 0.24, whereas in the cement matrix, the value increases to more than 0.4.[62]

In RRC (Figure 15D,E), the (Na+K)/Si ratio of ASR products rose as the Ca/Si ratio increased, spanning 0.2–0.5. The reason can be the greater alkali binding capacity of ASR products with a low Ca/Si ratio, as C-S-H gel with a lower Ca/Si ratio binds alkali more effectively than that with a higher Ca/Si ratio.[8] Moreover, alkalis serve as charge balancers during the process of aluminosilicate polymerization; therefore, the high-Al ASR gel cluster also

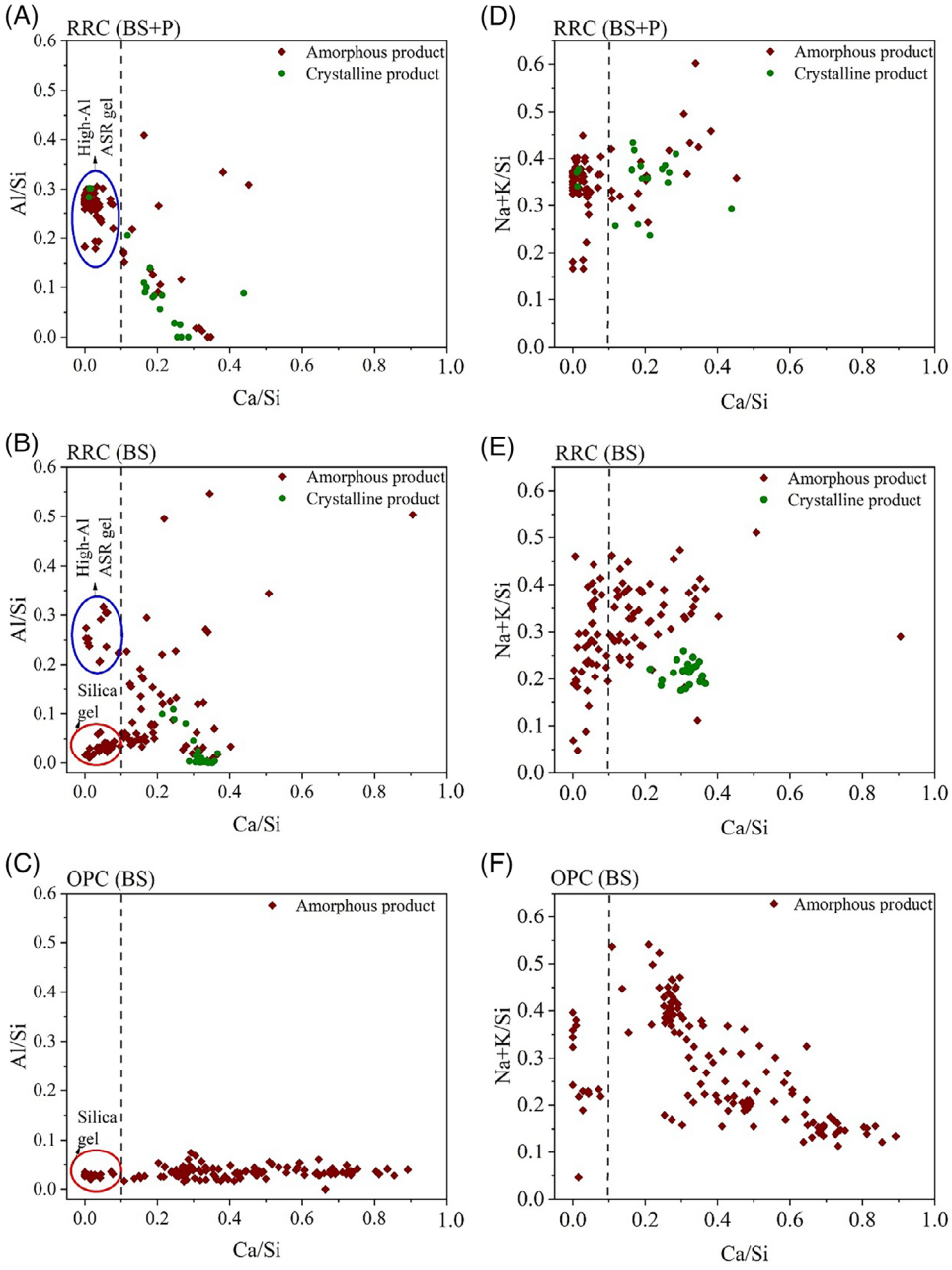

FIGURE 15 (Na+K)/Si versus Ca/Si in different ASR products in (A) RRC (BS+P), (B) RRC (BS), (C) OPC (BS), and Al/Ca versus Ca/Si in different ASR products in (D) RRC (BS+P), (E) RRC (BS), (F) OPC (BS).

showed alkali binding capability. Whereas, the (Na+K)/Si ratio of the ASR products in OPC decreased with the increase in the Ca/Si ratio (Figure 15F), indicating alkali recycling into the pore solution by Ca^{2+}.[18,63]

5 | DISCUSSION

Based on the findings of this study, a plausible mechanism for alkali–silica reaction in a lime-calcined clay binder (RRC) system is proposed and summarized in Figure 17. Calcined clay is an amorphous aluminosilicate,[12] where the Al dissolution is more favorable than that of Si.[64] These Al^{3+} ions can effectively facilitate silicate species condensation in alkali silicate solutions.[65] Additionally, nearly all the portlandite in the lime-clay binder is consumed within 7 days of hydration (Figure 3),[10] rendering it a low-calcium binder.

The schematic in Figure 17A illustrates that when RRC mortar containing amorphous, porous pumice (Figure 17A-i) is exposed to alkaline conditions, aggregate dissolution begins within the voids as the pore solution

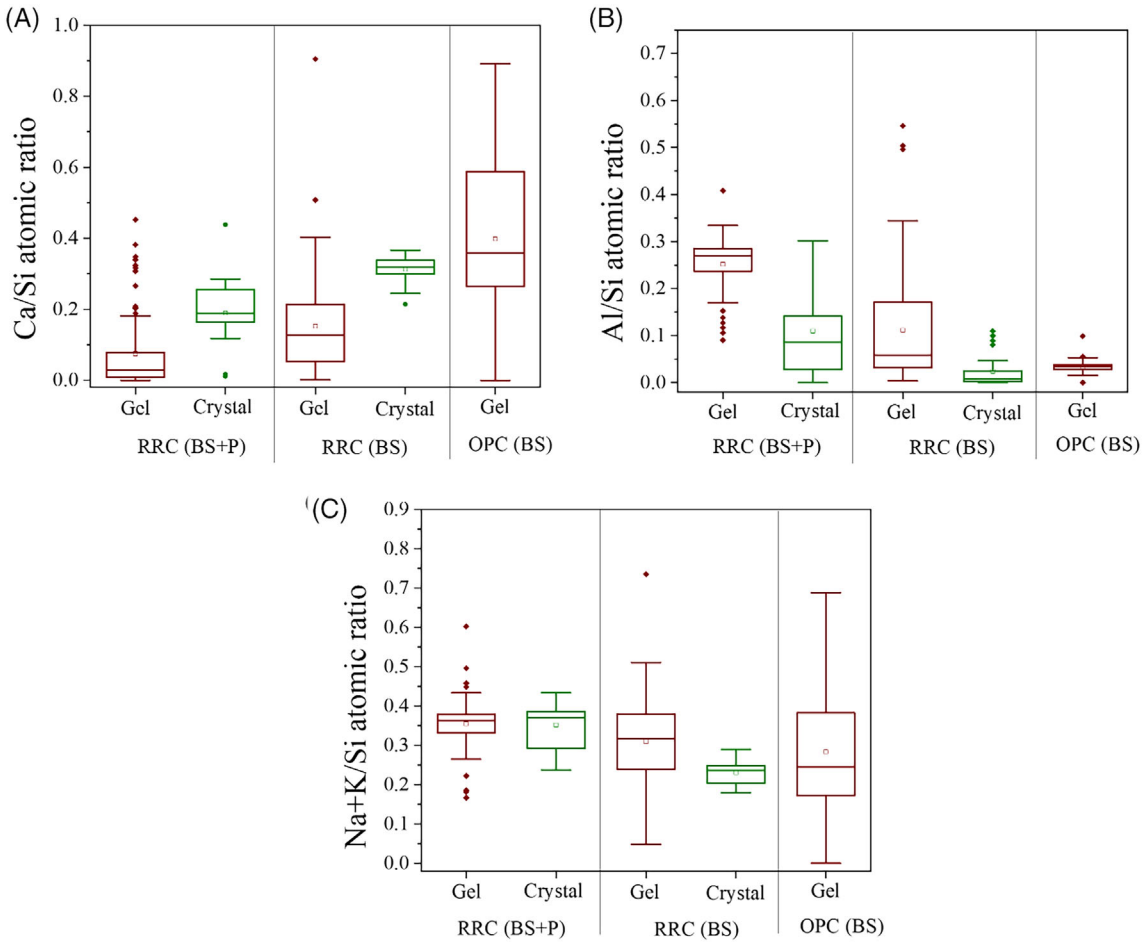

FIGURE 16 (A) Ca/Si, (B) Al/Ca, and (C) (Na+K)/Si ratio in different ASR products in different samples.

penetrates, introducing ions like Ca, Na, Si, and Al (Figure 17A-ii). This process promotes hydration products like C-A-S-H precipitation within the voids (Figure 17A-ii). As pumice dissolution progresses under the OH^- ion influence, Si and Al are released and hydrolyzed, leading to gelation and the N-A-S-H gel formation (Figure 17A-iii). During long-term alkaline exposure, the continuous Al and Si incorporation from pumice leads to two distinct phase formations: a high-Al ASR gel or zeolite phase near the vicinity of undissolved pumice, where Al and Si are abundant, and an ASR product in its core (Figure 17A-iv,v). Portlandite, used as the binder component to produce RRC, was observed to be consumed in forming Ca-bearing hydration products such as hydrocalumite, ettringite, gismondine, and stratlingite within 7 days (Figure 3A). Over the long term, these products release Ca^{2+}, which contributes to the formation of ASR gel. This ASR gel may have crystallized due to prolonged alkaline exposure. Moreover, the highly polymerized aluminosilicates or zeolites are not expensive and prevent further ASR gel formation by absorbing free silica.[66]

In RRC mortar with borosilicate aggregate, ASR reaction starts from the aggregate-binder matrix interface due to the absence of internal voids (Figure 17B-i). The reaction mechanism differs for precipitating ASR products outside or inside the aggregate. As OH^- ions initially dissolve the aggregate, released Si^{4+} ions bind with Na^+ to form sodium silicate (N-S-H) gel (Figure 17B-ii). At the ITZ between the aggregate and binder matrix, Al^{3+} and Ca^{2+} from the binder matrix interact with the initially formed N-S-H gel, stabilizing it into an N-A-S-H gel (Figure 17B-iii). N-S-H gel with minimal or no Al^{3+} and Ca^{2+} incorporation has low viscosity, which may cause it to leach out of the matrix or migrate into the binder matrix (Figure 17B-iii). Subsequently, it can either convert into high-Al ASR gel (N-A-S-H) by incorporating Al or form low-viscosity ASR gel by incorporating Ca (Figure 17B-iv). Ca incorporation into the ASR gel from borosilicate dissolution was higher than that observed in pumice due to the gel infiltrating the binder matrix and absorbing calcium (Figure 11E). Conversely, simultaneous Al and Ca intrusion, along with the silica dissolution, may promote the entire aggregate initially converting into a Ca-contained geopolymer-like gel

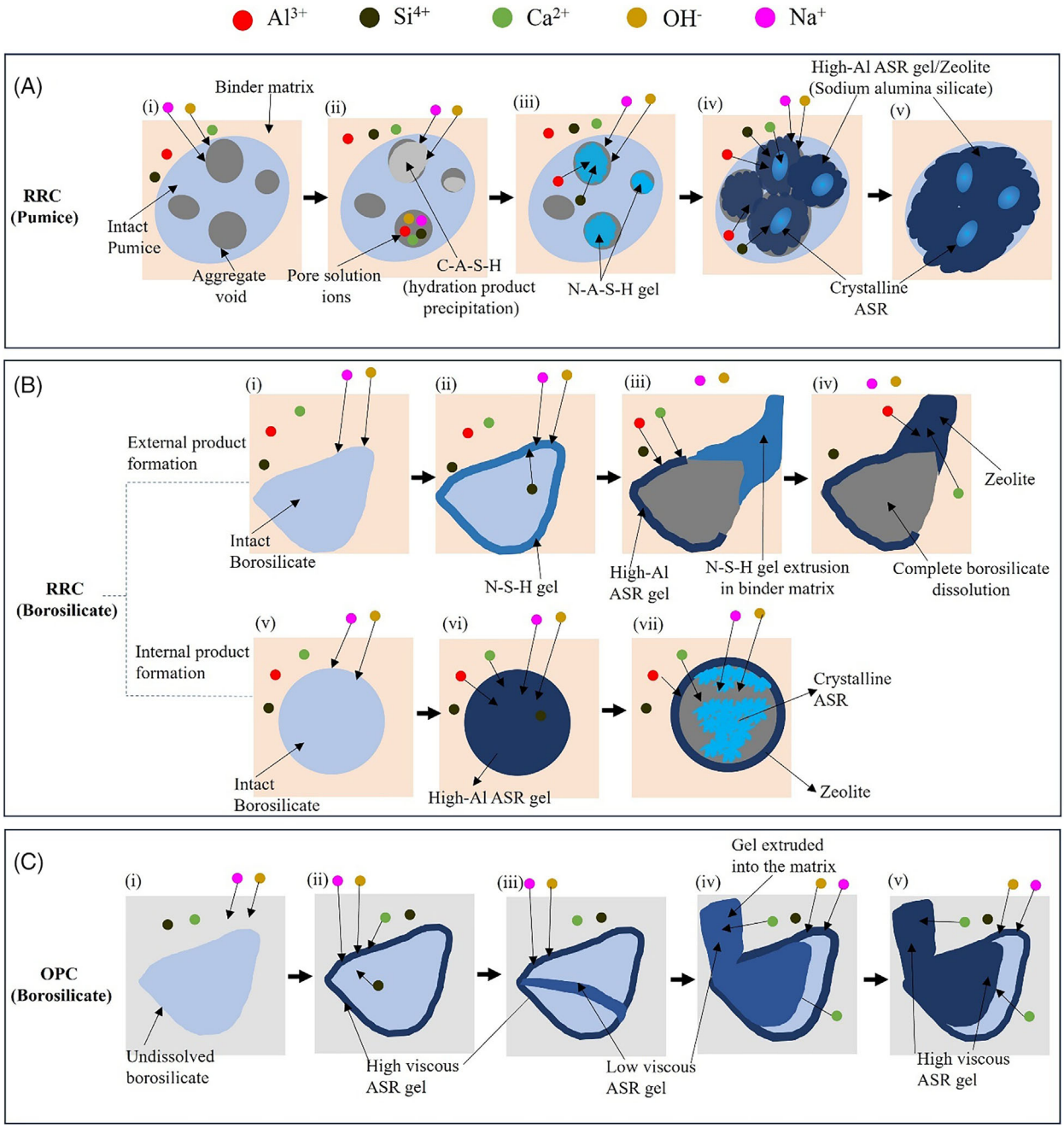

FIGURE 17 ASR product formation mechanism in (A) RRC-pumice sample, (B) RRC-borosilicate sample, and (C) OPC-borosilicate sample.

(Figure 17B-vi), later transforming into a crystalline ASR product (Figure 17B-vii).

Overall, the ASR expansion mitigation mechanism in the RRC matrix primarily depended on alumina polymerizing the dissolved silica from the aggregate, leading to zeolite formation rather than reducing silica dissolution. Under alkaline conditions, both pumice and borosilicate were fully dissolved: pumice transformed into sodium alumino silicate or zeolites at the reaction site (Figure 7E), while the less viscous alkali–silica gel from dissolved borosilicate either left the matrix or was polymerized by the Al in the RRC binder (Figure 11D,E). Krivenko et al.[32] also reported that the formation of a zeolite-like shell around aggregate particles due to reactions between alkali-susceptible aggregates and active alumina from metakaolin and fly ash in alkali-activated cements could inhibit the further progression of harmful ASR reactions. Additionally, the zeolite phase's alkali uptake capacity and the binder's low Ca content contributed to the mitigation, as evidenced by the low expansion (Figure 2) observed in

RRC-based mortars. Incorporating pumice as an aggregate was also observed to assist in mitigating ASR expansion due to having internal voids and active alumina availability. Lightweight aggregates, whether alkali-reactive or nonreactive, can reduce ASR damage by accommodating gel products in their voids.[38,39] Consequently, any crack formation caused by ASR product formation or crystallization of zeolites and ASR was prevented by accommodating these products within the voids of pumice, ultimately yielding a dense microstructure (Figure 6A). Pumice and other lightweight aggregates also decrease ASR expansion by providing alumina and consuming portlandite.[23,36,67]

The ASR product formation mechanism in the OPC system differs from that of RRC due to its high Ca and low Al content. According to the observations in Figure 14, the schematic for ASR in OPC is illustrated in Figure 17C. As silica dissolution from borosilicate initiates under alkaline conditions, Ca incorporation occurs, forming ASR gel at the boundary. Continuous Ca inclusion increases the gel viscosity (Figure 17C-ii), making it act like a semipermeable membrane that allows OH^- ions to penetrate but prevents Si diffusion from the reaction site.[57] Therefore, the low-viscosity ASR gel formed inside creates pressure on the aggregate, forms cracks, and propagates into it (Figure 17C-iii). This low-viscosity ASR gel lacks Ca, swells up, eventually creates cracks in the binder matrix, and extrudes into it (Figure 17C-iv). Subsequently, Ca gets incorporated into this low-viscosity ASR gel, transforming it into a homogeneous, high-viscosity ASR gel product (Figure 17C-v).

Lastly, in the RRC matrix with borosilicate aggregate (Figure 6B), microcracks likely formed due to shrinkage associated with the transformation of Al-rich ASR gel into zeolites, such as phillipsite and chabazite, as confirmed by XRD analysis. This process begins with the dissolution of silica from borosilicate at the outer regions of the sample under alkali exposure. The released silica reacts with alumina from the calcined clay, forming a polymerized network that, over time, converts into zeolites. This transformation can lead to localized shrinkage through a syneresis mechanism, resulting in visible microcracking. Such shrinkage cracks were absent in the RRC sample with pumice (Figure 6A), likely because zeolite formation occurred within the pumice's internal voids, reducing stress on the matrix due to zeolitic conversion and resulting in a denser structure. Despite the visible shrinkage cracks in the borosilicate-containing sample, expansion was limited. This is because the ASR gel formed in the RRC (BS) matrix did not incorporate significant amounts of calcium (Figure 15A,B), leading to a low-viscosity gel that could migrate away from the reaction site without causing expansion. In contrast, in the OPC matrix (Figure 6C), higher ASR expansion was observed due to the formation of ASR gel with a wide Ca/Si ratio (0.1–0.9) (Figure 15C). Consequently, high Ca availability forms a semipermeable C-S-H rim around the aggregate, allowing OH^- in but restricting the viscous and expansive low-Ca ASR gel from escaping, thereby creating internal pressure at the ITZ and causing noticeable cracking in the borosilicate grains.[31,32] Thus, while RRC (BS) shows more visible microcracks due to shrinkage during zeolite conversion, the actual expansion was lower compared with OPC, where expansive ASR gel formation is the dominant mechanism. Moreover, the ASR product formed in the RRC matrix exhibited higher alkali binding than that in the OPC matrix (Figure 15D–F), which also contributed to the reduced ASR expansion.[68]

6 | CONCLUSION

Based on the experimental results and discussions, the findings are summarized as follows:

(i) After 2 years of exposure to alkaline conditions, the ASR-induced expansion of the lime-calcined clay (RRC) samples was 0.02%, while OPC reached its maximum expansion limit of 0.1% within 7 days, resulting in a total expansion of 0.3% after 2 years.
(ii) The primary reaction products formed at this early stage included ettringite, hydrocalumite, gismondine, and gehlenite. However, during long-term alkali exposure, these calcium-bearing minerals disappeared, leaving primarily crystalline zeolites, with phillipsite and chabazite as the dominant phases in both RRC samples, along with the crystallized ASR product Na-shlykovite.
(iii) RRC sample containing pumice exhibited high resistance to alkaline attack, with a uniformly dense cross-section and minimal dissolution of borosilicates, whereas the RRC sample with borosilicate experienced complete dissolution only in the peripheral zone, leaving the core intact.
(iv) In RRC mortar, under alkaline exposure, pumice dissolution initiates within its internal voids, while borosilicate dissolution begins at the aggregate-binder matrix interface. Al availability in the pumice assists in the continuous incorporation of Al with N-S-H gel, forming zeolite inside the aggregate, whereas low-viscosity N-S-H gel from borosilicate dissolution can migrate and form zeolite inside the binder matrix.
(v) The high Al/Si ratio (~0.2–0.3) of the ASR products in RRC indicates the probable silica polymerization and zeolite formation. Moreover, these zeolites depicted a high-alkali-uptaking capacity by exhibiting a (Na+K)/Si ratio ranging from 0.2 to 0.5.

Future studies should consider adjusting aggregate proportions based on bulk density, as specified in ASTM C1260, to ensure consistent aggregate volume fractions across different systems. This will allow a more accurate assessment of aggregate reactivity by isolating the effect of mineralogy from volumetric differences. Moreover, the calcined clay used in this study was a blend of kaolinite and montmorillonite, with a kaolinite content of 75%, classifying it as high-grade clay. Also, the Al_2O_3 content in the kaolinite used here was 41% which is also high. It is expected that the low-quality clay will have a lesser availability of Al_2O_3, which played a crucial role in the ASR performance of the mortar batches. Therefore, the conclusions are not directly applicable to low-grade clay, and further investigation is needed to determine whether the conclusions hold when using low-grade clays.

ACKNOWLEDGMENTS

This work was conducted with funding from the Defense Advanced Research Projects Agency (DARPA, award #W911NF2010308). All opinions, findings, and conclusions or recommendations expressed in this material are those of the authors and do not necessarily reflect the views of the funding agencies.

ORCID

Adhora Tahsin https://orcid.org/0009-0001-6230-8911
Ishrat Baki Borno https://orcid.org/0000-0002-9912-8754
Taehwan Kim https://orcid.org/0000-0003-4371-7178
Warda Ashraf https://orcid.org/0000-0002-5867-5129

REFERENCES

1. Zhang Y, Zhang Q, Xue C, Wu K, Chang J, Lu J, et al. Influence of seawater concentration on alkali-silica reaction of seawater sea-sand concrete: mimicking through NaCl solution and recycled glass aggregate. Constr Build Mater. 2023;394:132110. https://doi.org/10.1016/j.conbuildmat.2023.132110
2. Zhang Y, Xu X, Zhao Q, Chang J, Ding S, Liu X, et al. Long-term investigation of alkali-silica reaction behaviors in seawater sea-sand concrete. Cem Concr Compos. 2024;151:105611. https://doi.org/10.1016/j.cemconcomp.2024.105611
3. Wu W, Wang T, Gong Q, Zhang K, An X, Wang D. Characteristics of the alkali-silica reaction in seawater and sea sand concrete with different water-cement ratios. Constr Build Mater. 2023;400:132822. https://doi.org/10.1016/j.conbuildmat.2023.132822
4. Santhanam M, Cohen M, Olek J. Differentiating seawater and groundwater sulfate attack in Portland cement mortars. Cem Concr Res. 2006;36(12):2132–37. https://doi.org/10.1016/j.cemconres.2006.09.011
5. Jackson MD, Mulcahy SR, Chen H, Li Y, Li Q, Chappelletti P, et al. Phillipsite and Al-tobermorite mineral cements produced through low-temperature water-rock reactions in Roman marine concrete. Am Mineral. 2017;102(7):1435–50. https://doi.org/10.2138/am-2017-5993CCBY
6. Brandon CJ, Hohlfelder RL, Jackson MD, JPeter O. Building for Eternity : The History and Technology of Roman Concrete Engineering in the Sea. Oxbow Books; 2014.
7. Ramasamy U, Bordelon AC, Tikalsky PJ. Properties of different pumice grades blended with cement. J Mater Civ Eng. 2017;29(7). https://doi.org/10.1061/(asce)mt.1943-5533.0001891
8. Kasaniya M, Thomas MDA, Moffatt EG. Efficiency of natural pozzolans, ground glasses and coal bottom ashes in mitigating sulfate attack and alkali-silica reaction. Cem Concr Res. 2021;149:106551. https://doi.org/10.1016/j.cemconres.2021.106551
9. Jackson MD, Oleson JP, Moon J, Zhang Y, Chen H, Gudmundsson MT. Extreme durability in ancient Roman concretes. Am Ceram Soc Bull. 2018;97(5):22–28. www.ceramics.org
10. Tahsin A, Siddique S, Ashraf W, Sattler M. Assessment of the durability and environmental impact of seawater-activated portlandite-calcined clay binder. J Sustain Cem Based Mater. 2023;12(12):1564–76. https://doi.org/10.1080/21650373.2023.2243480
11. Ashraf W, Borno IB, Khan RI, Siddique S, Haque MI, Tahsin A. Mimicking the cementation mechanism of ancient Roman seawater concrete using calcined clays. Appl Clay Sci. 2022;230:106696. https://doi.org/10.1016/j.clay.2022.106696
12. Fernandez R, Martirena F, Scrivener KL. The origin of the pozzolanic activity of calcined clay minerals: A comparison between kaolinite, illite and montmorillonite. Cem Concr Res. 2011;41(1):113–22. https://doi.org/10.1016/j.cemconres.2010.09.013
13. Seymour LM, Tamura N, Jackson MD, Masic A. Reactive binder and aggregate interfacial zones in the mortar of Tomb of Caecilia Metella concrete, 1C BCE, Rome. J Am Ceram Soc. 2022;105:1503–18. https://doi.org/10.1111/jace.18133
14. Brito A, García F, Álvarez C, Arvelo R, Fierro JLG, Díaz C. High surface area support/catalyst derived from natural pumice. Study of pretreatment variables. Ind Eng Chem Res. 2004;43(7):1659–64. https://doi.org/10.1021/ie020442e
15. Czapik P. Microstructure and degradation of mortar containing waste glass aggregate as evaluated by various microscopic techniques. Materials. 2020;13(9):2186. https://doi.org/10.3390/ma13092186
16. Wang W, Noguchi T, Tomoyose A, Zhang Y, Maruyama I. Influence of volcanic glass powder on alkali-silica reaction expansion in alkali-activated slag mortars. Cem Concr Compos. 2024;152:105665. https://doi.org/10.1016/j.cemconcomp.2024.105665
17. Shi Z, Shi C, Zhang J, Wan S, Zhang Z, Ou Z. Alkali-silica reaction in waterglass-activated slag mortars incorporating fly ash and metakaolin. Cem Concr Res. 2018;108:10–19. https://doi.org/10.1016/j.cemconres.2018.03.002
18. Rajabipour F, Giannini E, Dunant C, Ideker JH, Thomas MDA. Alkali-silica reaction: current understanding of the reaction mechanisms and the knowledge gaps. Cem Concr Res. 2015;76:130–46. https://doi.org/10.1016/j.cemconres.2015.05.024
19. Joo HE, Takahashi Y. Analytical and experimental studies on alkali-silica reaction mechanism: aggregate cracking and chemical composition change of gel. Cem Concr Compos.

2023;139:105003. https://doi.org/10.1016/j.cemconcomp.2023.105003

20. Hay R, Ostertag CP. On utilization and mechanisms of waste aluminium in mitigating alkali-silica reaction (ASR) in concrete. J Clean Prod. 2019;212:864–79. https://doi.org/10.1016/j.jclepro.2018.11.288
21. Hou X, Struble LJ, Kirkpatrick RJ. Formation of ASR gel and the roles of C-S-H and portlandite. Cem Concr Res. 2004;34(9):1683–96. https://doi.org/10.1016/j.cemconres.2004.03.026
22. Kim T, Alnahhal MF, Nguyen QD, Panchmatia P, Hajimohammadi A, Castel A. Initial sequence for alkali-silica reaction: transport barrier and spatial distribution of reaction products. Cem Concr Compos. 2019;104:103378. https://doi.org/10.1016/j.cemconcomp.2019.103378
23. Samimi K, Pakan M, Eslami J. Investigating the compressive strength and microstructural analysis of mortar containing synthesized graphene and natural pozzolan in the face of alkali-silica reactions. J Build Eng. 2023;68:106126. https://doi.org/10.1016/j.jobe.2023.106126
24. Fanijo EO, Kolawole JT, Almakrab A. Alkali-silica reaction (ASR) in concrete structures: mechanisms, effects and evaluation test methods adopted in the United States. Case Stud Constr Mater. 2021;15:e00563. https://doi.org/10.1016/j.cscm.2021.e00563
25. Krüger ME, Hilbig H, Stelzner L, Machner A. Effect of the chemical composition of synthetic alkali-silica gels on their structure, swelling behavior and water uptake. Cem Concr Res. 2024;184:107596. https://doi.org/10.1016/j.cemconres.2024.107596
26. Chatterji S. Chemistry of alkali-silica reaction and testing of aggregates. Cem Concr Compos. 2005;27(7-8):788–95. https://doi.org/10.1016/j.cemconcomp.2005.03.005
27. Leemann A, Góra M, Lothenbach B, Heuberger M. Alkali silica reaction in concrete—revealing the expansion mechanism by surface force measurements. Cem Concr Res. 2024;176:107392. https://doi.org/10.1016/j.cemconres.2023.107392
28. Hou X, Kirkpatrick RJ, Struble LJ, Monteiro PJM. Structural investigations of alkali silicate gels. J Am Ceram Soc. 2005;88(4):943–49. https://doi.org/10.1111/j.1551-2916.2005.00145.x
29. Wang H, Gillott JE. Mechanism of alkali-silica reaction and the significance of calcium hydroxide. Cem Concr Res. 1991;21:647–54.
30. Ichikawa T, Miura M. Modified model of alkali-silica reaction. Cem Concr Res. 2007;37(9):1291–97. https://doi.org/10.1016/j.cemconres.2007.06.008
31. Chatterji S, Jensen AD, Thaulow N, Christensen P. Studies of alkali-silica reaction. Part 3. Mechanisms by which NaCI and Ca(OH)2 affect the reaction. Cem Concr Res. 1986;16:246–254.
32. Krivenko P, Drochytka R, Gelevera A, Kavalerova E. Mechanism of preventing the alkali-aggregate reaction in alkali activated cement concretes. Cem Concr Compos. 2014;45:157–65. https://doi.org/10.1016/j.cemconcomp.2013.10.003
33. Shi Z, Lothenbach B. Role of aluminum and lithium in mitigating alkali-silica reaction—a review. Front Mater. 2022;8. https://doi.org/10.3389/fmats.2021.796396
34. Yang T, Zhang Z, Wang Q, Wu Q. ASR potential of nickel slag fine aggregate in blast furnace slag-fly ash geopolymer and Portland cement mortars. Constr Build Mater. 2020;262:119990. https://doi.org/10.1016/j.conbuildmat.2020.119990
35. Krüger ME, Heisig A, Hilbig H, Eickhoff H, Heinz D, Machner A. Effect of aluminum on the structure of synthetic alkali-silica gels. Cem Concr Res. 2023;166:107088. https://doi.org/10.1016/j.cemconres.2022.107088
36. Li C, Thomas MDA, Ideker JH. A mechanistic study on mitigation of alkali-silica reaction by fine lightweight aggregates. Cem Concr Res. 2018;104:13–24. https://doi.org/10.1016/j.cemconres.2017.10.006
37. Nguyen QD, Kim T, Castel A. Mitigation of alkali-silica reaction by limestone calcined clay cement (LC3). Cem Concr Res. 2020;137:106176. https://doi.org/10.1016/j.cemconres.2020.106176
38. Mo KH, Ling TC, Tan TH, Leong GW, Yuen CW, Shah SN. Alkali-silica reactivity of lightweight aggregate: a brief overview. Constr Build Mater. 2021;270:121444. https://doi.org/10.1016/j.conbuildmat.2020.121444
39. Yang S, Poon CS, Cui H. Alkali-silica reactivity of lightweight aggregates in alkali-activated slag cement and ordinary Portland cement systems. J Clean Prod. 2023;390:136187. https://doi.org/10.1016/j.jclepro.2023.136187
40. ASTM C1260. Standard test method for potential alkali reactivity of aggregates (Mortar-Bar method). ASTM International, West Conshohocken, PA, 2023.
41. ASTM C109. Standard test method for compressive strength of hydraulic cement mortars (using 2-in. or [50 mm] cube specimens). ASTM International, West Conshohocken, PA, 2024.
42. He R, Nantung T, (Luna) Lu N. Unraveling microstructural evolution in air-entrained mortar and paste: insights from MIP and micro-CT tomography amid cyclic freezing-thawing damage. J Build Eng. 2024;94:109922. https://doi.org/10.1016/j.jobe.2024.109922
43. Swamy R. The Alkali-Silica Reaction in Concrete. 1991. Accessed December 4, 2023. https://books.google.com/books?hl=en&lr=&id=p8-3BiBbYMC&oi=fnd&pg=PP1&ots=THEOmVPsnD&sig=KaXQCIKl20G5WAVRdM_hvrNvR_U
44. Duan W, Zhuge Y, Chow CWK, Keegan A, Liu Y, Merta I. Mitigation of alkali-silica reaction in blast-furnace slag-based alkaline activated material through incorporation of alum water treatment residue. Constr Build Mater. 2023;406:133383. https://doi.org/10.1016/j.conbuildmat.2023.133383
45. Archez J, Farges R, Gharzouni A, Rossignol S. Influence of the geopolymer formulation on the endogeneous shrinkage. Constr Build Mater. 2021;298:123813. https://doi.org/10.1016/j.conbuildmat.2021.123813
46. Frías M, Vigil de la Villa R, Martínez-Ramírez S, García-Giménez R, Sánchez de Rojas MI. Mineral phases in metakaolin-portlandite pastes cured 15 years at 60 °C. New data for scientific advancement. Appl Clay Sci. 2020;184:105368. https://doi.org/10.1016/j.clay.2019.105368
47. He P, Zhang B, Lu JX, Poon CS. ASR expansion of alkali-activated cement glass aggregate mortars. Constr Build Mater. 2020;261:119925. https://doi.org/10.1016/j.conbuildmat.2020.119925
48. Shi Z, Ma B, Lothenbach B. Effect of Al on the formation and structure of alkali-silica reaction products. Cem Concr Res. 2021;140:106311. https://doi.org/10.1016/j.cemconres.2020.106311

49. Ashraf W, Olek J. Carbonation behavior of hydraulic and non-hydraulic calcium silicates : potential of utilizing low-lime calcium silicates in cement-based materials. J Mater Sci. 2016;51(13):6173–91. https://doi.org/10.1007/s10853-016-9909-4
50. Haque MI, Borno IB, Khan RI, Ashraf W. Reducing carbonation degradation and enhancing elastic properties of calcium silicate hydrates using biomimetic molecules. Cem Concr Compos. 2023;136:104888. https://doi.org/10.1016/j.cemconcomp.2022.104888
51. Bernal SA, de Gutierrez RM, Provis JL, Rose V. Effect of silicate modulus and metakaolin incorporation on the carbonation of alkali silicate-activated slags. Cem Concr Res. 2010;40(6):898–907. https://doi.org/10.1016/j.cemconres.2010.02.003
52. Shi Z, Park S, Lothenbach B, Leemann A. Formation of shlykovite and ASR-P1 in concrete under accelerated alkali-silica reaction at 60 and 80°C. Cem Concr Res. 2020;137:106213. https://doi.org/10.1016/j.cemconres.2020.106213
53. Shi Z, Geng G, Leemann A, Lothenbach B. Synthesis, characterization, and water uptake property of alkali-silica reaction products. Cem Concr Res. 2019;121:58–71. https://doi.org/10.1016/j.cemconres.2019.04.009
54. Leemann A, Shi Z, Wyrzykowski M, Winnefeld F. Moisture stability of crystalline alkali-silica reaction products formed in concrete exposed to natural environment. Mater Des. 2020;195:109066. https://doi.org/10.1016/j.matdes.2020.109066
55. Borno IB, Tahsin A, Ashraf W. Utilization of industrial waste sodium sulfate for calcined clay-based sustainable binder. Constr Build Mater. 2024;440:137073. https://doi.org/10.1016/j.conbuildmat.2024.137073
56. Kapeluszna E, Kotwica Ł, Różycka A, Gołek Ł Incorporation of Al in C-A-S-H gels with various Ca/Si and Al/Si ratio: microstructural and structural characteristics with DTA/TG, XRD, FTIR and TEM analysis. Constr Build Mater. 2017;155:643–53. https://doi.org/10.1016/j.conbuildmat.2017.08.091
57. Shi Z, Lothenbach B. The role of calcium on the formation of alkali-silica reaction products. Cem Concr Res. 2019;126:105898. https://doi.org/10.1016/j.cemconres.2019.105898
58. Ma P, Li J, Bai J, Zhou Y, Chi L, Zhu Y, et al. Effect of type and quantity of inherent alkali cations on alkali-silica reaction. Cem Concr Res. 2023;173:107293. https://doi.org/10.1016/j.cemconres.2023.107293
59. Wang W, Maruyama I, Noguchi T. Impact of exposure conditions on alkali-silica reaction in alkali-activated material systems. Cem Concr Compos. 2024;153:105695. https://doi.org/10.1016/j.cemconcomp.2024.105695
60. Dilaria S, Secco M, Ghiotto AR, Furlan G, Giovanardi T, Zorzi F, et al. Early exploitation of Neapolitan pozzolan (pulvis puteolana) in the roman theatre of Aquileia, Northern Italy. Sci Rep. 2023;13(1):4110. https://doi.org/10.1038/s41598-023-30692-y
61. Hajimohammadi A, Provis JL, Van Deventer JSJ. The effect of silica availability on the mechanism of geopolymerisation. Cem Concr Res. 2011;41(3):210–16. https://doi.org/10.1016/j.cemconres.2011.02.001
62. Leemann A, Shi Z, Lindgård J. Characterization of amorphous and crystalline ASR products formed in concrete aggregates. Cem Concr Res. 2020;137:106190. https://doi.org/10.1016/j.cemconres.2020.106190
63. Kawabata Y, Yamada K. The mechanism of limited inhibition by fly ash on expansion due to alkali–silica reaction at the pessimum proportion. Cem Concr Res. 2017;92:1–15. https://doi.org/10.1016/j.cemconres.2016.11.002
64. Deng G, He Y, Lu L, Hu S. The effect of activators on the dissolution characteristics and occurrence state of aluminum of alkali-activated metakaolin. Constr Build Mater. 2020;235:117451. https://doi.org/10.1016/j.conbuildmat.2019.117451
65. Weng L, Sagoe-Crentsil K, Brown T, Song S. Effects of aluminates on the formation of geopolymers. Mater Sci Eng B. 2005;117(2):163–68. https://doi.org/10.1016/j.mseb.2004.11.008
66. Hünger KJ. The contribution of quartz and the role of aluminum for understanding the AAR with greywacke. Cem Concr Res. 2007;37(8):1193–205. https://doi.org/10.1016/j.cemconres.2007.05.009
67. Tapan M. Use of pumice and scoria aggregates for controlling alkali silica reaction. Physicochem Probl Miner Process. 2014;50(2):467–75. https://doi.org/10.5277/ppmp140204
68. Thomas M. The effect of supplementary cementing materials on alkali-silica reaction: A review. Cem Concr Res. 2011;41(12):1224–31. https://doi.org/10.1016/j.cemconres.2010.11.003

SUPPORTING INFORMATION

Additional supporting information can be found online in the Supporting Information section at the end of this article.

How to cite this article: Tahsin A, Borno IB, Kim T, Ashraf W. Understanding of alkali–silica reaction in lime-pozzolana mortar incorporating pumice and borosilicate. J Am Ceram Soc. 2025;108:e70168. https://doi.org/10.1111/jace.70168